Measurement of the production cross-section of positive pions in p–Al collisions at 12.9 GeV/c

HARP Collaboration

February 5, 2008

Abstract

A precision measurement of the double-differential production cross-section, $d^2\sigma^{\pi^+}/dpd\Omega$, for pions of positive charge, performed in the HARP experiment is presented. The incident particles are protons of 12.9 GeV/c momentum impinging on an aluminium target of 5% nuclear interaction length. The measurement of this cross-section has a direct application to the calculation of the neutrino flux of the K2K experiment. After cuts, 210 000 secondary tracks reconstructed in the forward spectrometer were used in this analysis. The results are given for secondaries within a momentum range from 0.75 GeV/c to 6.5 GeV/c, and within an angular range from 30 mrad to 210 mrad. The absolute normalization was performed using prescaled beam triggers counting protons on target. The overall scale of the cross-section is known to better than 6%, while the average point-to-point error is 8.2%.

Accepted for publication in Nucl. Phys. B

HARP collaboration

M.G. Catanesi, M.T. Muciaccia, E. Radicioni, S. Simone

Università degli Studi e Sezione INFN, Bari, Italy

R. Edgecock, M. Ellis[1], S. Robbins[2,3], F.J.P. Soler[4]

Rutherford Appleton Laboratory, Chilton, Didcot, UK

C. Gößling, M. Mass

Institut für Physik, Universität Dortmund, Germany

S. Bunyatov, A. Chukanov, D. Dedovitch, A. Elagin, M. Gostkin, A. Guskov, D. Khartchenko, O. Klimov, A. Krasnoperov, D. Kustov, K. Nikolaev, B. Popov[5], V. Serdiouk, V. Tereshchenko, A. Zhemchugov

Joint Institute for Nuclear Research, JINR Dubna, Russia

E. Di Capua, G. Vidal–Sitjes[6,1]

Università degli Studi e Sezione INFN, Ferrara, Italy

A. Artamonov[7], P. Arce[8], S. Giani, S. Gilardoni[6], P. Gorbunov[7], A. Grant, A. Grossheim[6], P. Gruber[6], V. Ivanchenko[9], A. Kayis-Topaksu[10], L. Linssen, J. Panman, I. Papadopoulos, J. Pasternak[6], E. Tcherniaev, I. Tsukerman[7], R. Veenhof, C. Wiebusch[3], P. Zucchelli[11,12]

CERN, Geneva, Switzerland

A. Blondel, S. Borghi, M. Campanelli, A. Cervera–Villanueva, M.C. Morone, G. Prior[6,13], R. Schroeter

Section de Physique, Université de Genève, Switzerland

I. Kato[14], T. Nakaya[14], K. Nishikawa[14], S. Ueda[14]

University of Kyoto, Japan

V. Ableev, U. Gastaldi

Laboratori Nazionali di Legnaro dell' INFN, Legnaro, Italy

G. B. Mills[15]

Los Alamos National Laboratory, Los Alamos, USA

J.S. Graulich[16], G. Grégoire

Institut de Physique Nucléaire, UCL, Louvain-la-Neuve, Belgium

M. Bonesini, M. Calvi, A. De Min, F. Ferri, M. Paganoni, F. Paleari

Università degli Studi e Sezione INFN, Milano, Italy

M. Kirsanov

Institute for Nuclear Research, Moscow, Russia

A. Bagulya, V. Grichine, N. Polukhina

P. N. Lebedev Institute of Physics (FIAN), Russian Academy of Sciences, Moscow, Russia

V. Palladino

Università "Federico II" e Sezione INFN, Napoli, Italy

L. Coney[15], D. Schmitz[15]

Columbia University, New York, USA

G. Barr, A. De Santo[17], C. Pattison, K. Zuber[18]

Nuclear and Astrophysics Laboratory, University of Oxford, UK

F. Bobisut, D. Gibin, A. Guglielmi, M. Laveder, A. Menegolli, M. Mezzetto

Università degli Studi e Sezione INFN, Padova, Italy

J. Dumarchez, S. Troquereau, F. Vannucci

LPNHE, Universités de Paris VI et VII, Paris, France

V. Ammosov, V. Gapienko, V. Koreshev, A. Semak, Yu. Sviridov, V. Zaets

Institute for High Energy Physics, Protvino, Russia

U. Dore

Università "La Sapienza" e Sezione INFN Roma I, Roma, Italy

D. Orestano, M. Pasquali, F. Pastore, A. Tonazzo, L. Tortora

Università degli Studi e Sezione INFN Roma III, Roma, Italy

C. Booth, C. Buttar[4], P. Hodgson, L. Howlett

Dept. of Physics, University of Sheffield, UK

M. Bogomilov, M. Chizhov, D. Kolev, R. Tsenov

Faculty of Physics, St. Kliment Ohridski University, Sofia, Bulgaria

S. Piperov, P. Temnikov

Institute for Nuclear Research and Nuclear Energy, Academy of Sciences, Sofia, Bulgaria

M. Apollonio, P. Chimenti, G. Giannini, G. Santin[19]

Università degli Studi e Sezione INFN, Trieste, Italy

Y. Hayato[14], A. Ichikawa[14], T. Kobayashi[14]

KEK, Tsukuba, Japan

J. Burguet–Castell, J.J. Gómez–Cadenas, P. Novella, M. Sorel, A. Tornero

Instituto de Física Corpuscular, IFIC, CSIC and Universidad de Valencia, Spain

[1]Now at Imperial College, University of London, UK.
[2]Now at Bergische Universität Wuppertal, Germany.
[3]Jointly appointed by Nuclear and Astrophysics Laboratory, University of Oxford, UK.
[4]Now at University of Glasgow, UK.
[5]Also supported by LPNHE (Paris).
[6]Supported by the CERN Doctoral Student Programme.
[7]Permanently at ITEP, Moscow, Russian Federation.
[8]Permanently at Instituto de Física de Cantabria, Univ. de Cantabria, Santander, Spain.
[9]On leave of absence from the Budker Institute for Nuclear Physics, Novosibirsk, Russia.
[10]On leave of absence from Çukurova University, Adana, Turkey.
[11]On leave of absence from INFN, Sezione di Ferrara, Italy.
[12]Now at SpinX Technologies, Geneva, Switzerland.
[13]Now at Lawrence Berkeley National Laboratory, Berkeley, USA.
[14]K2K Collaboration.
[15]MiniBooNE Collaboration.
[16]Now at Section de Physique, Université de Genève, Switzerland, Switzerland.
[17]Now at Royal Holloway, University of London, UK.
[18]Now at University of Sussex, Brighton, UK.
[19]Now at ESA/ESTEC, Noordwijk, The Netherlands.

1 Introduction

The objective of the HARP experiment is a systematic study of hadron production for beam momenta from 1.5 GeV/c to 15 GeV/c for a large range of target nuclei [1]. The main motivations are: a) to measure pion yields for a quantitative design of the proton driver of a future neutrino factory, b) to improve substantially the calculation of the atmospheric neutrino flux and c) to provide input for the flux calculation of accelerator neutrino experiments, such as K2K and MiniBooNE.

The measurement described in this paper is of particular relevance in the context of the recent results presented by the K2K experiment [2, 3], which have shown evidence for neutrino oscillations at a confidence level of four standard deviations. The K2K experiment uses an accelerator-produced ν_μ beam with an average energy of 1.3 GeV directed at the Super-Kamiokande detector. The K2K analysis compares the observed ν_μ spectrum in Super-Kamiokande, located at a distance of about 250 km from the neutrino source, with the predicted spectrum in the absence of oscillations. This, in turn, is computed by multiplying the observed spectrum at the near detector (located at 300 m from the neutrino source) by the so-called 'far–near ratio', R, defined as the ratio between the predicted flux at the far and near detectors. This factor corrects for the fact that at the near detector, the neutrino source is not point-like, but sensitive to effects such as the finite size of the decay tunnel, etc., whereas at the Super-Kamiokande site the neutrino source can be considered as point-like. According to the neutrino oscillation parameters measured in atmospheric neutrino experiments [4] the distortion of the spectrum measured with the far detector is predicted to be maximal in the energy range between 0.5 and 1 GeV. The determination of R is the leading energy-dependent systematic error in the K2K analysis [2, 3].

The HARP experiment has a large acceptance in the momentum and angular range relevant for K2K neutrino flux. It covers 80% of the total neutrino flux in the near detector and in the relevant region for neutrino oscillations. Thus, it can provide an independent, and more precise, measurement of the pion yield needed as input to the calculation of the K2K far–near ratio than that currently available.

The neutrino beam of the K2K experiment originates from the decay of light hadrons, produced by exposing an aluminium target to a proton beam of momentum 12.9 GeV/c. In this paper, the measurement of the double-differential cross-section, $d^2\sigma^{\pi^+}/dpd\Omega$ of positive pion production for protons of 12.9 GeV/c momentum impinging on a thin Al target of 5% nuclear interaction length ($\lambda_{\rm I}$) is presented, *i.e.* reproducing closely the conditions of the K2K beam-line for the production of secondaries.

The HARP apparatus [1, 5] is a large-acceptance spectrometer consisting of a forward and large-angle detection system. The forward spectrometer covers polar angles up to 250 mrad which is well matched to the angular range of interest for the K2K beam line.

The results reported here are based on data taken in 2002 in the T9 beam of the CERN PS. About 3.4 million incoming protons were selected. After cuts, 209 929 secondary tracks reconstructed in the forward spectrometer were used in this analysis. The results are given in the region relevant for K2K, that is the momentum range from 0.75 GeV/c to 6.5 GeV/c and within an angular range from 30 mrad to 210 mrad. The absolute normalization was performed using 280 542 'minimum-bias' triggers.

This paper is organized as follows. The experimental apparatus is outlined in Section 2. Section 3 describes tracking with the forward spectrometer. Section 4 discusses the calculation of the reconstruction efficiency. Section 5 summarizes the particle identification (PID) capabilities of the spectrometer and describes the PID algorithm. Sections 6 and 7 give details of the cross-section calculation. Results are discussed in Section 8. A comparison with previous data is presented in Section 9. An illustrative calculation of the K2K far–near ratio is shown in Section 10. A summary is given in Section 11.

2 Experimental apparatus

The HARP detector, shown in Fig. 1, consists of forward and large-angle detection systems. The convention used for the coordinate system is also given in the Figure. In the large-angle region a TPC positioned in a solenoidal magnet is used for tracking. The forward spectrometer is built around a dipole

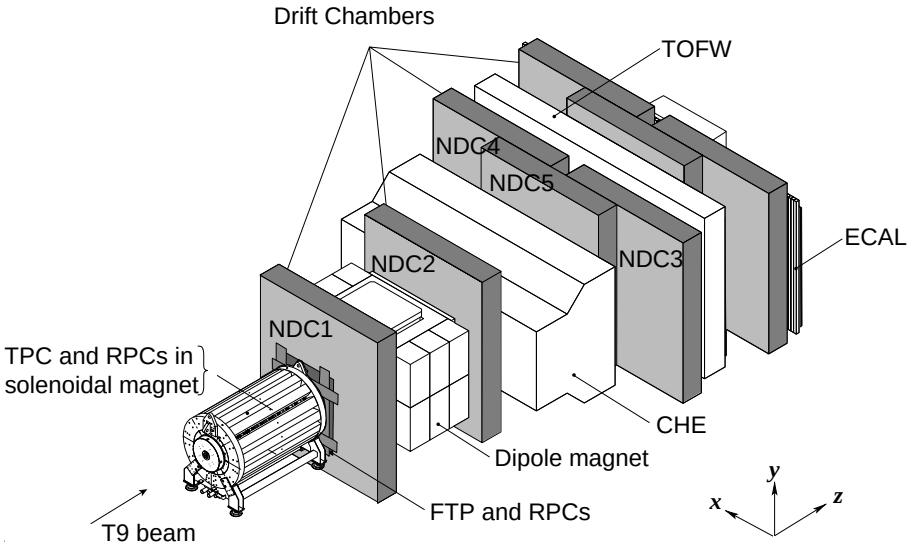

Figure 1: Schematic layout of the HARP spectrometer. The convention for the coordinate system is shown in the lower-right corner. The three most downstream (unlabelled) drift chambers are only partly equipped with electronics and not used for tracking.

magnet with an integral field of $\int B_y dL$=0.66 T m for momentum analysis, with large planar drift chambers (NDC) for particle tracking, and three detectors used for particle identification: a time-of-flight wall (TOFW), a threshold Cherenkov detector (CHE), and an electromagnetic calorimeter (ECAL). The target itself is located inside the TPC. Beam instrumentation, including three timing detectors (BTOF) and two threshold Cherenkov detectors (BCA and BCB), provides identification of the incoming particle and the determination of the interaction time at the target. The impact point of the beam particle on the target and its direction are measured by a set of multi-wire proportional chambers (MWPCs). Several trigger detectors are available to select events with an interaction and to define the normalization.

Data were taken with several beam momenta and target configurations. In addition to the data taken with the thin aluminium target of 5% λ_{I} at an incident proton momentum of 12.9 GeV/c, runs were also taken with an empty target holder. These data allow a subtraction to be made of the interactions occurring in the material on the path of the incident beam. Other relevant configurations for the measurement described here are the data taken with and without target with other beam momenta (1.5, 3.0, 5.0, 8.0, 8.9 and 15 GeV/c) with electrons, pions and protons. These settings have been used to determine the response of the spectrometer to these particles in terms of efficiency, momentum resolution and particle identification capability. Data with thick Al targets, such as a replica of the K2K target, have also been taken, but are not yet used in the present analysis. The momentum definition of the T9 beam is known with a precision of the order of 1% [6].

A detailed description of the HARP experiment is given in Ref. [5]. In this analysis we utilize primarily the detector components of the forward spectrometer and the beam instrumentation. Below, the elements which are important for this analysis will be mentioned.

2.1 Beam and trigger detectors

A schematic picture of the equipment in the beam line is shown in Fig. 2. It is instrumented with the following systems:

- A set of four multi-wire proportional chambers (MWPCs) measures the position and direction of the incoming beam particles, with an accuracy of ≈1 mm in position and ≈0.2 mrad in angle per projection.

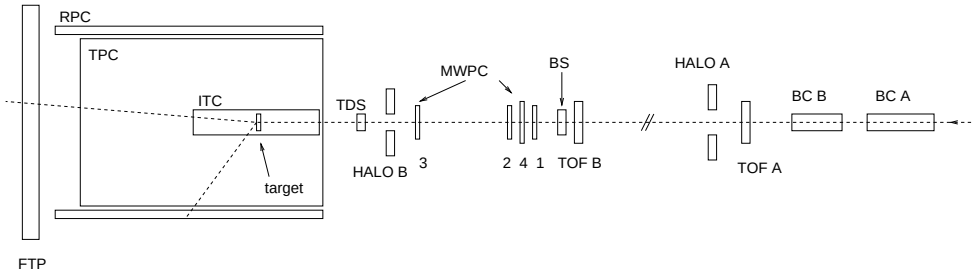

Figure 2: Schematic view of the trigger and beam equipment. The description is given in the text. The beam enters from the right. The MWPCs are numbered: 1, 4, 2, 3 from right to left. On the left, the position of the target inside the inner field cage of the TPC is shown.

- A beam time-of-flight system (BTOF) measures time difference over a distance of 21.4 m. It is made of two identical scintillation hodoscopes, TOFA and TOFB (originally built for the NA52 experiment [7]), which, together with a small target-defining trigger counter (TDS, also used for the trigger and described below), provide particle identification at low energies. This allows separation of pions, kaons and protons up to 5 GeV/c and provides the initial time at the interaction vertex (t_0). The resolution is shown in Fig. 3. The t_0, *i.e.* the time at which the incident beam particle is predicted to cross the mid-plane of the target ($z = 0$), is calculated after particle identification. The weighted average of the individual measurements of t_0 from the three timing detectors is calculated, taking into account the velocity, β, of the particle using the known beam momentum and the particle mass deduced after identification. The timing resolution of the combined BTOF system is about 70 ps.

- A system of two N_2-filled Cherenkov detectors (BCA and BCB) is used to tag electrons at low energies and to tag pions at higher energies. The electron and pion tagging efficiency is found to be close to 100%. At momenta larger than 12 GeV/c it is also possible to tag kaons as can be seen in Fig. 4 which shows the pulse height spectrum of BCA and BCB for a 12.9 GeV/c beam. This spectrum displays raw channel counts without pedestal subtraction (the pedestal is around channel 110). The kaon and pion peaks can be clearly distinguished from the pedestal peak at low pulse-height which is due to heavier particles below Cherenkov threshold such as protons. The electrons are part of the pion peak.

The target is positioned inside the inner field cage of the TPC. It has a cylindrical shape with a nominal diameter of 30 mm. The aluminium (99.999% pure) target used for the measurement described here has a nominal thickness of 5% λ_{I}. Precise measurements of the thickness have been performed at different locations on its surface and show a maximum variation between 19.73 mm and 19.85 mm.

A set of trigger detectors completes the beam instrumentation: a thin scintillator slab covering the full aperture of the last quadrupole magnet in the beam line to start the trigger logic decision (BS); a small scintillator disk, TDS mentioned above, positioned upstream of the target to ensure that only particles hitting the target cause a trigger; and 'halo' counters (scintillators with a hole to let the beam particles pass) to veto particles too far away from the beam axis.

The TDS is designed to have a very high efficiency (measured to be 99.9%). It is located as near as possible to the entrance of the TPC and has a 20 mm diameter, smaller than the target which has a 30 mm diameter. Its time resolution ($\sim$ 130 ps) is sufficiently good to be used as an additional detector for the BTOF system.

A double plane of scintillation counters (FTP), positioned upstream of the dipole magnet, is used to select events with an interaction in the target and outgoing charged particles in the forward region. The plane covers the full aperture of the dipole magnet, with the exception of a central hole with a diameter of 60 mm to let the beam particles pass. The efficiency of the FTP was measured using events which had been taken simultaneously using triggers which did not require the FTP and amounts to >99.8%.

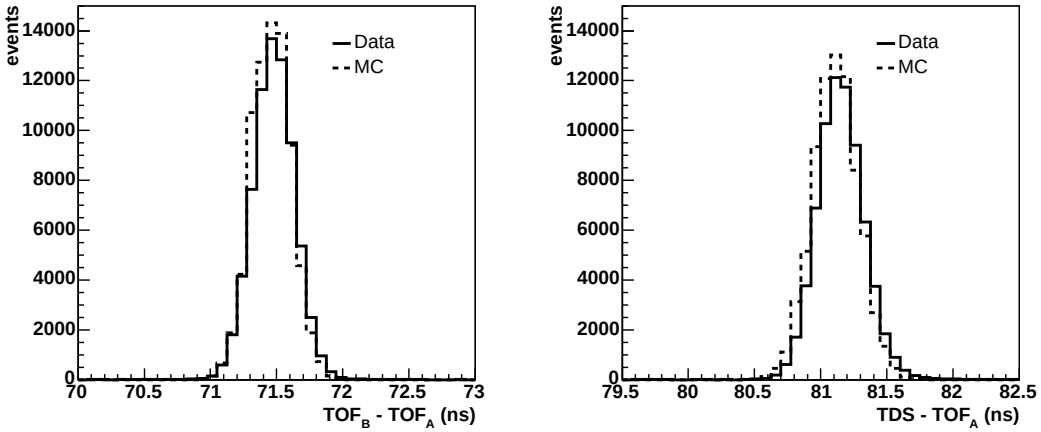

Figure 3: The timing resolution of the beam TOF detectors. The left hand panel shows the time difference measured between TOFA and TOFB, the right hand panel the time difference between TDS and TOFA.

2.2 Drift chambers

The main tracking device of the HARP forward spectrometer is a set of large drift chambers (NDC) placed upstream and downstream of the dipole magnet. These chambers were originally built for the NOMAD experiment [8], where they served both as a target for neutrino interactions and as a tracker for the produced charged particles.

The spectrometer contains five NDC modules, each of which is made of four chambers. The chambers consist of three wire planes, with one plane (x) of wires oriented vertically; the other two (u and v) are rotated with respect to the vertical by ± 5 degrees. They have been described elsewhere [9] and we refer to [5] for a detailed description of their performance under HARP conditions. This performance can be summarized in terms of two quantities, spatial resolution and hit efficiency per plane. After internal alignment of the individual wires, the spatial resolution of the chamber is about 340 μm. The hit efficiency is smaller in HARP than it was in NOMAD due to the use of a different, non-flammable but less efficient gas mixture. The hit efficiency varies between 80% and 85% in the central NDC modules.

2.3 PID detectors

Particle identification is performed in the forward spectrometer through the combination of several detectors downstream of the dipole magnet (CHE, TOFW and ECAL). We refer to [5] for a detailed description of the three systems.

A large scintillator wall (TOFW) covering the full acceptance of the downstream tracking system is used in conjunction with the timing information from the beam detectors to measure the time-of-flight of the secondary particles for momenta up to 5 GeV/c. The TOFW measures the time-of-flight of particles emanating from the target, and this, together with the charged track trajectory length, l, determines the velocity, β, of the particle.

The single scintillator counters are BC408 bars from Bicron, 2.5 cm thick and 21 cm wide. The counters are grouped into three mechanical structures (palisades). In the left and right palisades, scintillators are 250 cm long and are mounted vertically, while in the central palisade scintillators are 180 cm long and are mounted horizontally. The counters overlap partially by 2.5 cm to ensure full coverage. The scintillator slabs are viewed by one photo-multiplier tube (Philips XP2020) at each side. The TOFW and its performance is described in detail in Ref. [10]. With an intrinsic resolution of the individual counters of 160 ps, a time-of-flight resolution better than 180 ps is achieved using this detector in combination

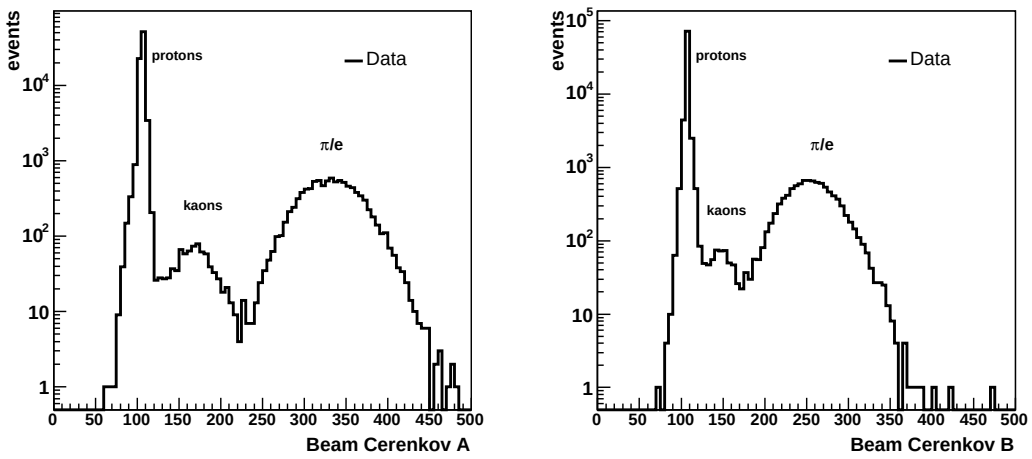

Figure 4: Pulse height spectra expressed in ADC counts from beam Cherenkov counters BCA (left) and BCB (right) at 12.9 GeV/c. The pedestal (marked 'protons' representing particles with a velocity below threshold) is around channel 110 in both cases.

with the BTOF system.

The threshold Cherenkov detector (CHE) separates pions from protons for momenta above the pion threshold (2.6 GeV/c) and identifies electrons below the pion threshold. The radiator gas (perfluorobutane C_4F_{10}) is chosen for its high refractive index, which allows the detector to be operated at atmospheric pressure. The particles traverse about 2 m of the radiating medium and generate photons that are deflected by about 135° upward or downward by two large cylindrical mirrors 6 m long with a radius of curvature of 2.4 m. Thirty-eight EMI 9356-KA photo-multipliers were used for their very low noise and high gain characteristics. In order to increase their useful light-collection area to a diameter of 340 mm, the photo-multipliers were matched to aluminized Winston cones.

Finally, the electromagnetic calorimeter (ECAL) provides electron rejection. It is segmented longitudinally into two planes. The two calorimeter planes were assembled from existing calorimeter modules of the CHORUS experiment [11]. These planes consist of 62 and 80 modules, covering a total active width of 4.96 m and 6.4 m, respectively. Each module is composed of scintillating fibres (1 mm diameter) embedded in extruded lead sheets with a volume ratio 1/4. The ratio of the energy deposition in the two planes is different for electrons compared to hadrons. In addition, the comparison of the momentum of the particle measured by the curvature of its trajectory and the energy deposition in the calorimeter provides another way to identify electrons. The ECAL complements the electron rejection of the Cherenkov above the pion Cherenkov threshold.

3 Tracking with the forward spectrometer

3.1 Tracking algorithm

The track reconstruction algorithm starts by building two-dimensional (2D) segments per NDC module. Those are later combined to create 3D track segments (also per module). The requirements are the following:

- *Plane (2D) segment*: At least three hits out of four in the same projection (u, x or v) compatible with being aligned. The drift sign associated to each hit is decided during the plane segment reconstruction phase.

- *Track (3D) segment*: Two or three plane segments of different projections, whose intersection defines a 3D straight line. In the case where only two plane segments are found, an additional hit in the remaining projection is required. This hit must intersect the 3D straight line defined by the other two projections.

Consequently, to form a track segment at least seven hits (from a total of 12 measurement planes) are needed within the same NDC module. Once track segments are formed in the individual modules they are combined (downstream of the dipole magnet) to obtain longer track segments. Finally, downstream tracks are connected with either the interaction vertex or a 3D track segment in NDC1 (the NDC module upstream the dipole magnet, see Fig. 1) to measure the momentum. All these tasks are performed by a sophisticated fitting, extrapolation and matching package called RecPack [12], which is based on the well known Kalman Filter technique [13].

The interaction vertex in this analysis is well defined. The transverse coordinates (x, y) are obtained by extrapolating the trajectory of the incoming beam particle, measured with the MWPCs (with an error of the order of 1 mm), and the z coordinate can be taken as that of the nominal plane of the target (which is 19.80 mm thick).

Consequently, the momentum of a track can be determined by imposing the constraint that it emanates from the vertex, that is, by connecting a 3D segment downstream the dipole magnet with a 3D point upstream the magnet. Tracks of this type are called 'VERTEX2 tracks', and the estimator of the momentum obtained by connecting a 3D segment with the vertex 3D point is denoted 'p_2'. Specifically, this is done by extrapolating the downstream 3D segment to the nominal plane of the target, and imposing that the distance between the transverse coordinates thus obtained (x_s, y_s) and the (x, y) coordinates defined above is less than 10 cm (in practice one builds a χ^2 which also takes into account the measurement errors). Tracks which extrapolate to distances larger than 10 cm are not considered (in fact, the inefficiency of the p_2 algorithm, a few percent comes almost exclusively from this source).

Alternatively, one can measure the momentum connecting a 3D segment downstream of the dipole with a 3D segment in the NDC1 module. These are called 'VERTEX4 tracks', and the estimator of the momentum is denoted 'p_4'. The way a downstream segment is connected with a NDC1 3D segment is described with some detail below. In essence, one requires a reasonable collinearity in the non-bending plane and obtains the momentum from the curvature in the bending plane.

The availability of two independent momentum estimators allows the tracking efficiency to be measured from the data themselves. This is possible, since, a) the reconstruction methods providing the estimators p_2 and p_4 are independent b) p_2 and p_4 have a Gaussian distribution around the true momentum p (The distribution is expected to be Gaussian in the variable $1/p$ rather than p. With the relatively good resolution the difference is negligible.) This makes it possible to use one of the estimators (p_2) to measure the yields while the other (p_4) is used to measure tracking efficiency. The estimator p_2 is preferred to measure yields since it does not involve the use of the NDC1 module, where tracking efficiency is lower than in the downstream modules (see the discussion on tracking efficiency in Section 4).

Figure 5 shows the inclusive p_2 distribution measured for events with an FTP trigger. The hole in the FTP largely suppresses the peak of beam protons at 12.9 GeV/c. The remaining peak corresponds to events with an FTP trigger caused by elastically scattered protons, protons with multiple scattering in the tail of the angular distribution, and by protons accompanied by soft particles produced upstream of the FTP. The linear correlation between p_2 and p_4, shown in Fig. 6 (left panel) for simulated tracks, illustrates the fact that both are estimators of the same quantity, while the correlation between p_4 and p (Fig. 6, right panel) shows that both are unbiased estimators of p. The small non-linearities and disagreements between p_2 and p_4 and between p_4 and p have negligible contribution to the total systematic uncertainty.

3.2 Momentum and angular resolution

Following the previous discussion, the momentum measurement for VERTEX2 tracks is performed by extrapolating tracks built downstream of the magnet to the vertex plane. The algorithm performs a loop over allowed momenta. For each value of p one computes the extrapolated position (x_t, y_t) at the

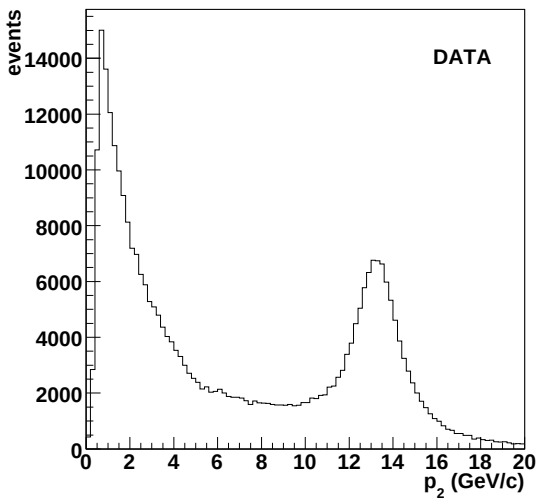

Figure 5: Inclusive p_2 momentum distribution of reconstructed tracks (see text for definition). The peak from non-interacting beam particles is visible at 12.9 GeV/c.

target reference z_0 coordinate and the matching χ^2 with the event (x_0, y_0) coordinates. The momentum is then calculated by minimizing this χ^2. For VERTEX4 the algorithm is similar, but in this case, a 3D segment downstream of the magnet is matched to a 3D segment in NDC1 module. In both cases, an upper cut on the minimum matching χ^2 decides whether the matching is accepted or not. This reduces the background from tertiary particles (not coming from the primary vertex) in the case of matching with the vertex (VERTEX2 tracks). For VERTEX4, this cut reduces the background from particles interacting in the region between NDC1 and NDC2.

The momentum resolution as a function of the momentum is shown in Fig. 7 (left panel), for the case of p_2. The resolution can be measured using beam particles of several momenta. Also shown (open circles) is the corresponding resolution found using the Monte Carlo.

The momentum resolution does not improve below 3 GeV/c due to details of the momentum reconstruction algorithm and also because the particles traverse the material at larger angles so that the multiple scattering term is no longer a constant. This feature is well reproduced by the simulation. Figure 7 (right panel), shows the angular resolution. Both the momentum and angular resolutions are small compared with the size of the bins used in this analysis (500 MeV/c momentum bins, up to 4 GeV/c, 1000 MeV/c from 4 to 5 GeV/c, 1500 MeV/c from 5 to 6.5 GeV/c, and 30 mrad angular bins). In the region of interest, the agreement between data and Monte Carlo is good for the momentum resolution, while for the angular resolution the difference is less than 1 mrad, negligible compared to the bin size. Thus effects due to the finite resolution are small, and it is safe to apply a Monte Carlo based correction.

The charge misidentification rate has been estimated by computing the fraction of protons that are reconstructed with negative charge. This is done by measuring the fraction of negative particles with momenta above the pion CHE threshold that give no signal in CHE. The upper limit of 0.5% for the charge misidentification probability is found to be consistent with the known CHE inefficiency.

3.3 Definition of kinematical variables

The final cross section, being rotationally invariant around the beam axis, can be expressed in polar coordinates (p, θ), where p is the true total momentum of the particle and θ is the true angle with respect to the beam axis (approximately equivalent to the z axis). However, given the rectangular geometry of the dipole and of the drift chambers, some of the corrections needed to compute the cross-section are

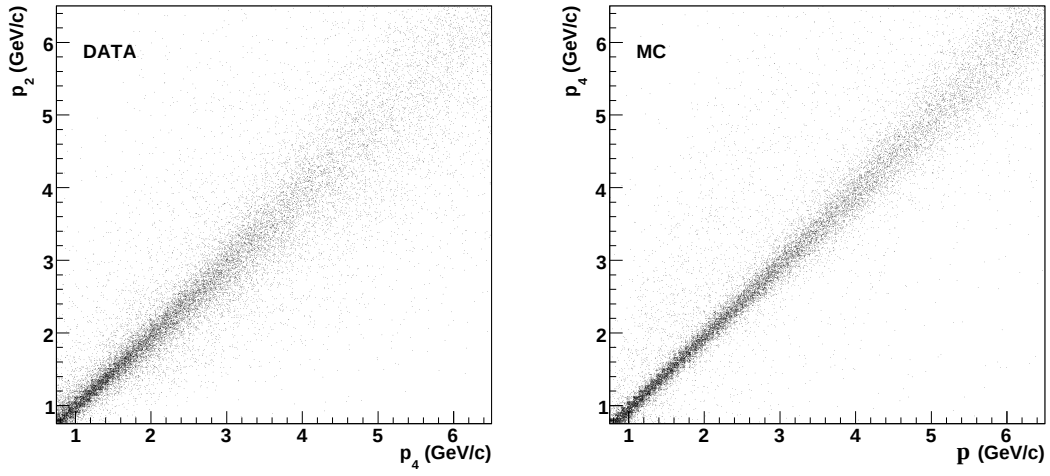

Figure 6: Left panel: The correlation between p_2 and p_4, showing that both are estimators of the same quantity; right panel: the correlation between p_4 and p shows that p_4 is an unbiased estimator of the momentum p within the momentum resolution and binning (from 500 MeV/c up to 1.5 GeV/c) used in the analysis.

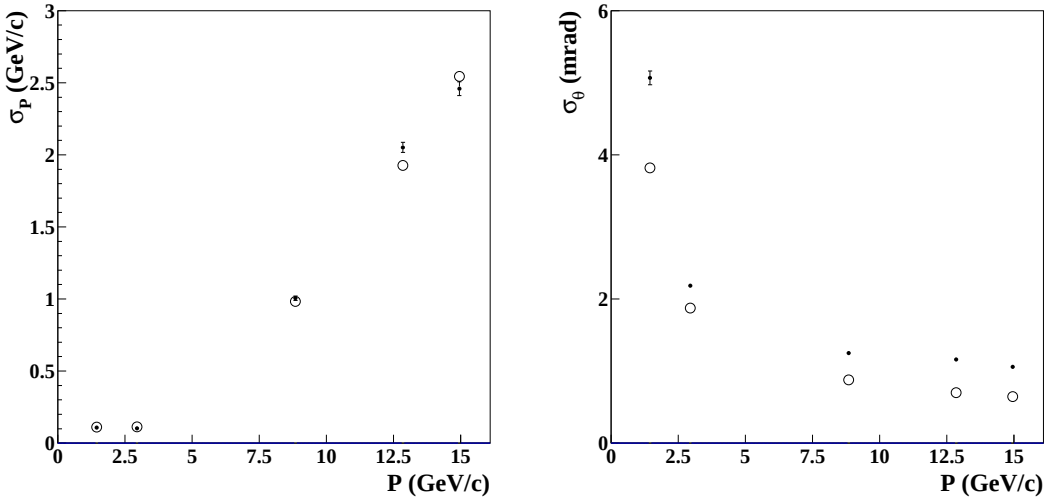

Figure 7: Left panel: momentum resolution (p_2) obtained from fits to data (points with error bars) taken using several well-defined discrete beam momenta and no target. Also shown (open circles) is the corresponding resolution found using the Monte Carlo. Right panel: angular resolution obtained from fits to data (points with error bars) taken using several well-defined discrete beam momenta and no target. The open circles show again the corresponding resolution found using the Monte Carlo. In the region of interest, the agreement between data and Monte Carlo is good for momentum resolution with values much smaller than the binning used in the analysis (from 500 MeV/c for $p < 4$ GeV/c up to 1.5 GeV/c at $p = 6.5$ GeV/c). Similarly the difference between measured and predicted angular resolution is negligible compared to the 30 mrad binning adopted in the analysis (see text).

most naturally expressed in terms of (p, θ_x, θ_y), where $\theta_x = \arctan(p_x/p_z)$ and $\theta_y = \arctan(p_y/p_z)$. Thus the conversion from rectangular to polar coordinates is carried out at a later stage of the analysis.

4 Track reconstruction efficiency

The track reconstruction efficiency, $\varepsilon^{\text{track}}(p, \theta_x, \theta_y)$, is defined as the fraction of tracked particles (with position and momentum measured) N^{track} with respect to the total number of particles N^{parts} reaching the fiducial volume of the HARP spectrometer as a function of the true momentum, p, and angles, θ_x, θ_y:

$$\varepsilon^{\text{track}}(p, \theta_x, \theta_y) = \frac{N^{\text{track}}(p, \theta_x, \theta_y)}{N^{\text{parts}}(p, \theta_x, \theta_y)} \ . \tag{1}$$

The track reconstruction efficiency can be computed using the redundancy of the drift chambers taking advantage of the multiple techniques used for the track reconstruction. The rest of this section details the steps leading to this calculation. The efficiency was calculated for positively charged particles only.

4.1 The use of the p_4 estimator to measure tracking efficiencies

The calculation of the cross-section requires the knowledge of tracking efficiency and acceptance in terms of the true kinematical variables of the particle. Strictly speaking, this is only possible if one uses the Monte Carlo to compute these quantities. This would make the calculation sensitive to the details of the Monte Carlo simulation of the spectrometer.

The existence of two independent estimators of the momentum allows the tracking efficiency to be measured in terms of p_4, taking advantage of the fact that it is Gaussian distributed around p and therefore can be used to approximate the latter.

Therefore, a sample of p_4 tracks is selected with well measured momentum imposing the additional constraint that the tracks emanate from the primary vertex. This is achieved by requiring that the distance of the track extrapolation to the MWPC vertex is smaller than 10 mm. By construction, the vertex of VERTEX2 tracks clusters at a small radius around the nominal vertex origin (defined by the MWPC resolution) which is fully covered by these VERTEX4 tracks.

4.2 Module efficiency

Using the selected sample of VERTEX4 tracks, one can measure the tracking efficiency and acceptance of individual NDC modules in terms of VERTEX4 kinematical quantities.

The measurement of p_2 requires a downstream segment which is then connected to the event vertex. In turn, a downstream segment can be made of a segment in NDC2, or a segment in any of the modules downstream NDC2 (that is NDC3, NDC4 and NDC5, see Fig. 8). For the purpose of the analysis one can treat *conceptually* those three NDC modules as a single module which we call *back-plane*. Thus, a downstream segment is defined as a NDC2 segment, a back-plane segment or a long segment which combines both NDC2 and back-plane. In all cases the measurement of p_2 requires that the true particle has crossed NDC2. By definition the control sample of VERTEX4 tracks verifies that the true particle crossed NDC2 (since the measurement of p_4 requires a downstream segment connected to NDC1), but not necessarily that a segment was reconstructed in NDC2 (since a good VERTEX4 track can be built with a back-plane segment and a segment in NDC1). In practice, the required condition is that at least six hits are found inside the road defined by the extrapolation of the downstream track to NDC2. It was verified that this condition has a negligible effect on the efficiency determination.

The NDC2 efficiency ε_2 is defined as the number of segments reconstructed in NDC2 (in terms of VERTEX4 kinematical quantities, p, θ_x, θ_y) divided by the number of tracks in the VERTEX4 control sample.

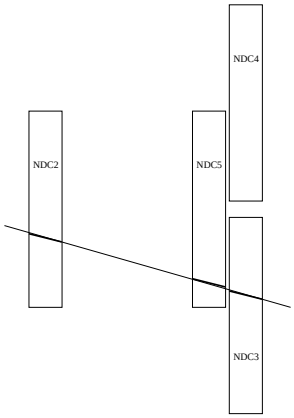

Figure 8: Schematic layout of the downstream modules of the drift chambers (top view).

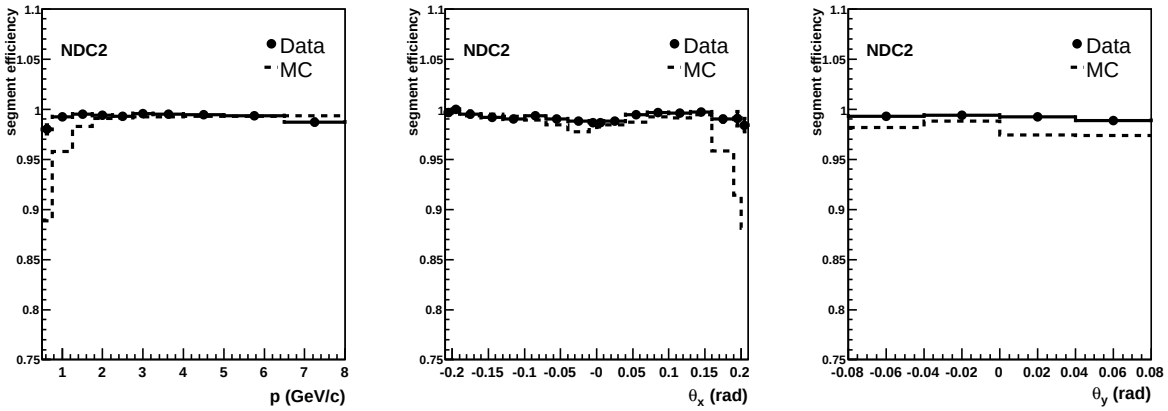

Figure 9: Segment efficiency of NDC2 module (see text for definition), as a function of p (left panel), θ_x (centre panel) and θ_y (right panel). The efficiency is computed as a three-dimensional function of the above variables. The plots show the individual projections. Points with error bars correspond to data, the dashed line to Monte Carlo. The agreement between Monte Carlo and data calculation is good except in the region of large θ_x and small p (see text).

This is equivalent to finding the number of segments reconstructed in NDC2 divided by the number of particles reaching NDC2. Thus ε_2 measures the 'true' tracking efficiency of the NDC2 module, unfolded from other effects such as acceptance, absorption or decay. If a particle decays or is absorbed before reaching NDC2 it will not be included in the control sample and therefore it will not be included in the calculation of ε_2.

Figure 9 shows ε_2 as a function of p, θ_x, θ_y (estimated from the VERTEX4 control sample). As expected the distribution is flat in terms of all three variables. The dots represent the calculation from the data themselves, and show that the NDC2 tracking efficiency is essentially 100%. The dashed line represents the Monte Carlo calculation, which agrees with the data calculation except in the region of low momentum and large, positive θ_x. The inefficiencies in these regions are correlated and are due to edge effects which are not perfectly described in the Monte Carlo. This region is not used in the analysis.

The back-plane efficiency, ε_b, is defined as the number of segments reconstructed in the back-plane divided by the number of tracks in the VERTEX4 control sample. This definition folds tracking efficiency with acceptance and other effects such as absorption or decay (for example, one could have a well reconstructed VERTEX4 track with a NDC2 segment and a NDC1 segment, decaying or undergoing

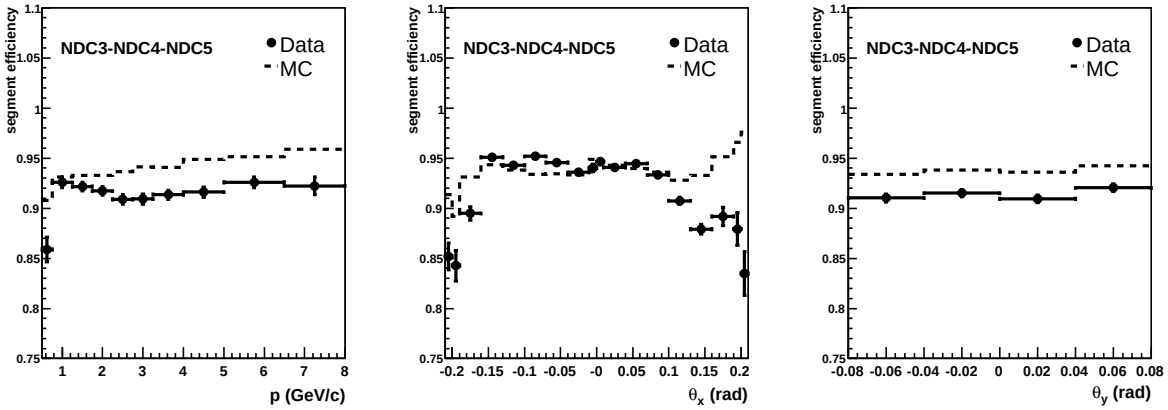

Figure 10: Segment efficiency of the back-plane, defined by modules NDC3, NDC4 and NDC5 shown as a function of p (left panel), θ_x (center panel) and θ_y (right panel). The efficiency is computed as a three-dimensional function of the above variables. The plots show the individual projections. Points with error bars correspond to data, the dashed line to Monte Carlo.

a nuclear interaction in NDC2). The Monte Carlo tends to overestimate the efficiency by less than 5% on average (see Fig. 10). At large positive θ_x the Monte Carlo predicts a rise in the efficiency which is not seen in the data. This is a region where large angle tracks are further deflected by the magnet and traverse the drift chambers at large angles. As will be shown below, owing to the redundancy of the chambers, the overall downstream efficiency is well reproduced by the simulation.

The knowledge of the efficiency of NDC1 is not needed, since the yields are computed in terms of p_2 which does not use it. However, one could choose to measure the yields in terms of p_4 and use p_2 as an estimator of true momentum to measure tracking efficiency. In that case, NDC1 would play the same role that NDC2 plays in the current approach.

Indeed, it is illustrative to compute ε_1 for VERTEX4 tracks in terms of VERTEX2 kinematical quantities, p_2, θ_x, θ_y). The efficiency ε_1 is defined as the number of segments reconstructed in NDC1 divided by the number of tracks in a VERTEX2 control sample. This is equivalent to requiring the number of segments reconstructed in NDC1 over the number of particles reaching NDC1. Thus ε_1 measures the 'true' tracking efficiency of the NDC1 module, unfolded from other effects such as acceptance, absorption or decay.

Figure 11 shows ε_1 as a function of p, θ_x, θ_y (estimated from the VERTEX2 control sample). The distribution is relatively flat in θ_y, while it has a marked dependence on θ_x, with a minimum at $\theta_x = 0$. The distribution of ε_1 as a function of θ_x shows the inefficiency of NDC1 associated with a saturation of the chambers due to the primary beam intensity. NDC1 is the only module affected by this saturation effect, which is negligible downstream of the dipole magnet (as proved by inspection of ε_2). The Monte Carlo tends to overestimate the efficiency by 15%. The dip in the efficiency at θ_x close to the origin is induced by the saturation effect of the beam. This feature is simulated in the Monte Carlo by artificialy lowering the efficiency of the drift regions most traversed by undeflected beam particles. Although one can measure the NDC1 tracking efficiency with good precision using the data, the marked dependence on θ_x (which translates also in a dependence on p) suggests as a better strategy to measure the yields in terms of VERTEX2, which does not use NDC1.

4.3 Downstream tracking efficiency

The downstream tracking efficiency, $\varepsilon^{\rm down}$, is defined as the number of tracks reconstructed downstream the dipole magnet (those include NDC2 single segments, back-plane single segments and NDC2-back-plane combined segments) divided by the number of particles reaching NDC2 (which defines the fiducial

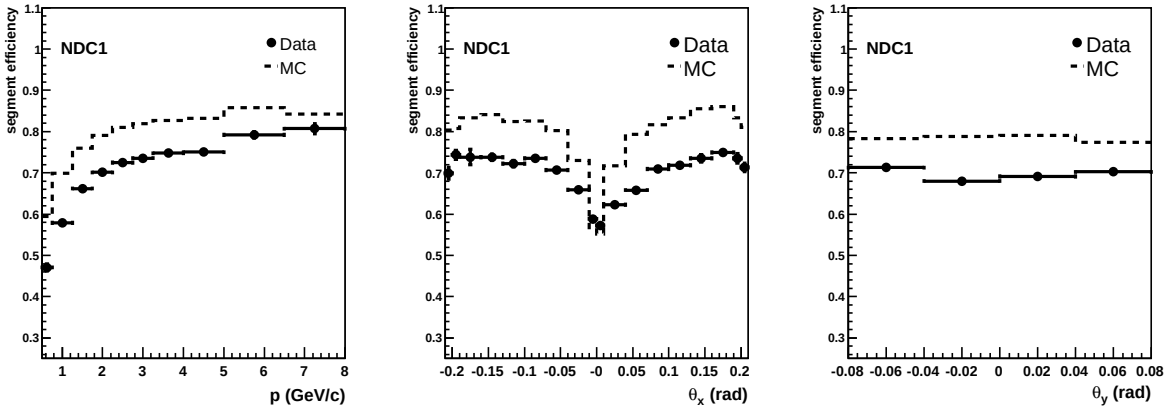

Figure 11: Segment efficiency of NDC1 (see text for definition) as a function of p (left panel), θ_x (center panel) and θ_y (right panel). The efficiency is computed as a three-dimensional function of the above variables. The plots show the individual projections. Points with error bars correspond to data, the dashed line to Monte Carlo.

volume). Since ε_2 and ε_b are uncorrelated, this quantity is easily computed from the individual segment efficiency described above, as:

$$\varepsilon^{\text{down}} = \varepsilon_2 + \varepsilon_b - \varepsilon_2 \cdot \varepsilon_b \ . \tag{2}$$

Figure 12 shows the total downstream segment efficiency in terms of the kinematical quantities (from VERTEX4) p, θ_x, θ_y. Due to the very high tracking efficiency of the individual modules (the apparent drop of the efficiency of the back-plane visible in Fig. 10 is largely due to decay and absorption) the downstream tracking efficiency is almost 100%, flat in all variables, within the angular acceptance considered. The overall downstream tracking efficiency is well reproduced by the Monte Carlo.

4.4 Upstream tracking efficiency

For the contribution of the vertex matching to the overall track reconstruction efficiency, one needs to compute the fraction of times that a good downstream track segment was correctly matched to the vertex point resulting in an acceptable momentum. This is also done using a VERTEX4 control sample, with the additional constraint that the particle emanates from the target volume. The latter condition is ensured by requiring $r_{\text{V4}} \leq 30$ mm, $\chi^2_{\text{match}} \leq 10$, where r_{V4} is the distance of the track extrapolation to the MWPC vertex in the target reference plane, and χ^2_{match} the goodness of the matching of the track with the beam particle track extrapolated to the nominal target position. The cut in χ^2_{match} guarantees good matching with the vertex. These tracks enter the denominator of the efficiency calculation. The numerator is made of the accepted VERTEX2 tracks within this sample:

$$\varepsilon^{\text{vertex2}} = \frac{N^{\text{vertex2}}(\exists p_2; \exists p_4, r_{\text{V4}} \leq 30 \text{ mm}, \chi^2_{\text{match}} \leq 10)}{N^{\text{vertex4}}(\exists p_4, r_{\text{V4}} \leq 30 \text{ mm}, \chi^2_{\text{match}} \leq 10)} \ , \tag{3}$$

where the condition $\exists p_{4(2)}$ guarantees that the track momentum was estimated by the two reconstruction algorithms, respectively.

The efficiency for reconstructing a VERTEX2 track for a particle coming from the target is shown in Fig. 13. Figure 13 (upper-left), shows that the efficiency as a function of θ_x is flat and close to 95%, up to 150 mrad and drops above this value. This drop is due a the momentum-dependent acceptance

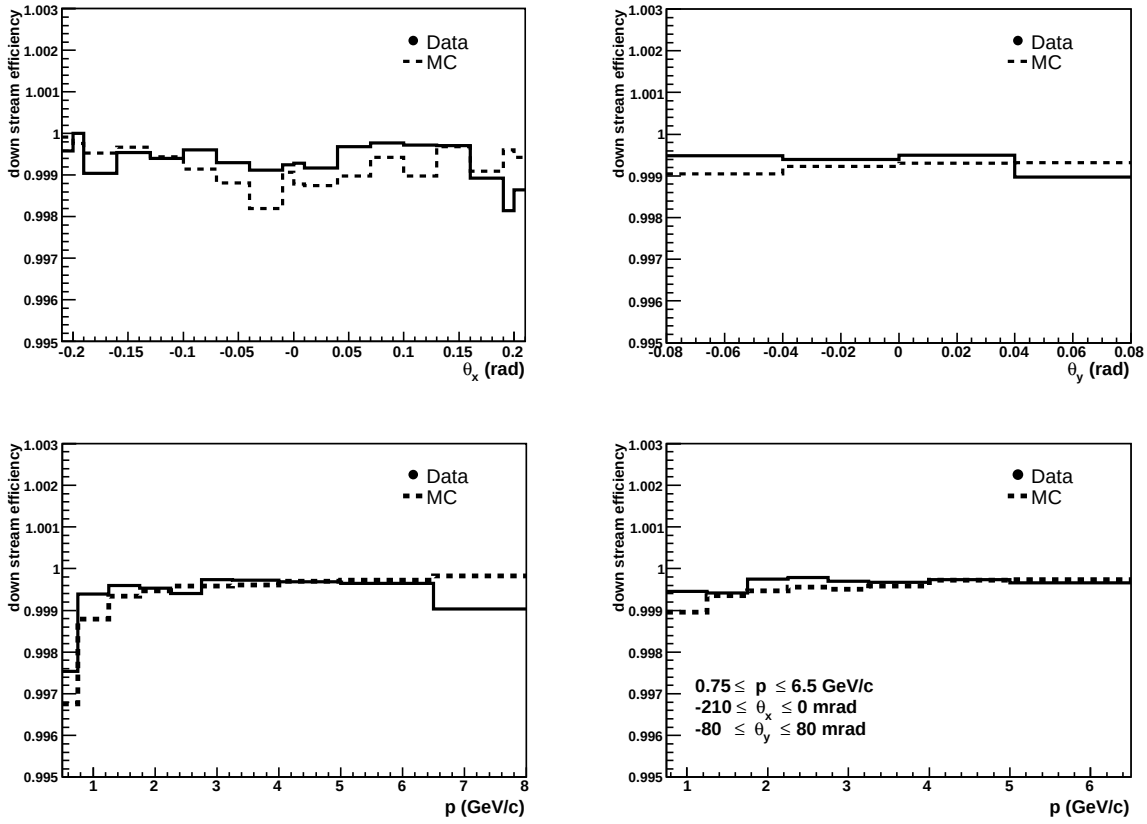

Figure 12: Downstream tracking efficiency as a function of kinematic variables, p, θ_x, and θ_y, at production for positively charged particles emanating from the vertex. Upper-left panel: As a function of θ_x. Upper-right panel: As a function of θ_y. Lower-left panel: As a function of p. Lower-right panel: As a function of p averaged over the θ_x and θ_y regions used in the present analysis only. The efficiency is flat in all variables and close to 100%. The solid histograms correspond to data, the dashed line to Monte Carlo.

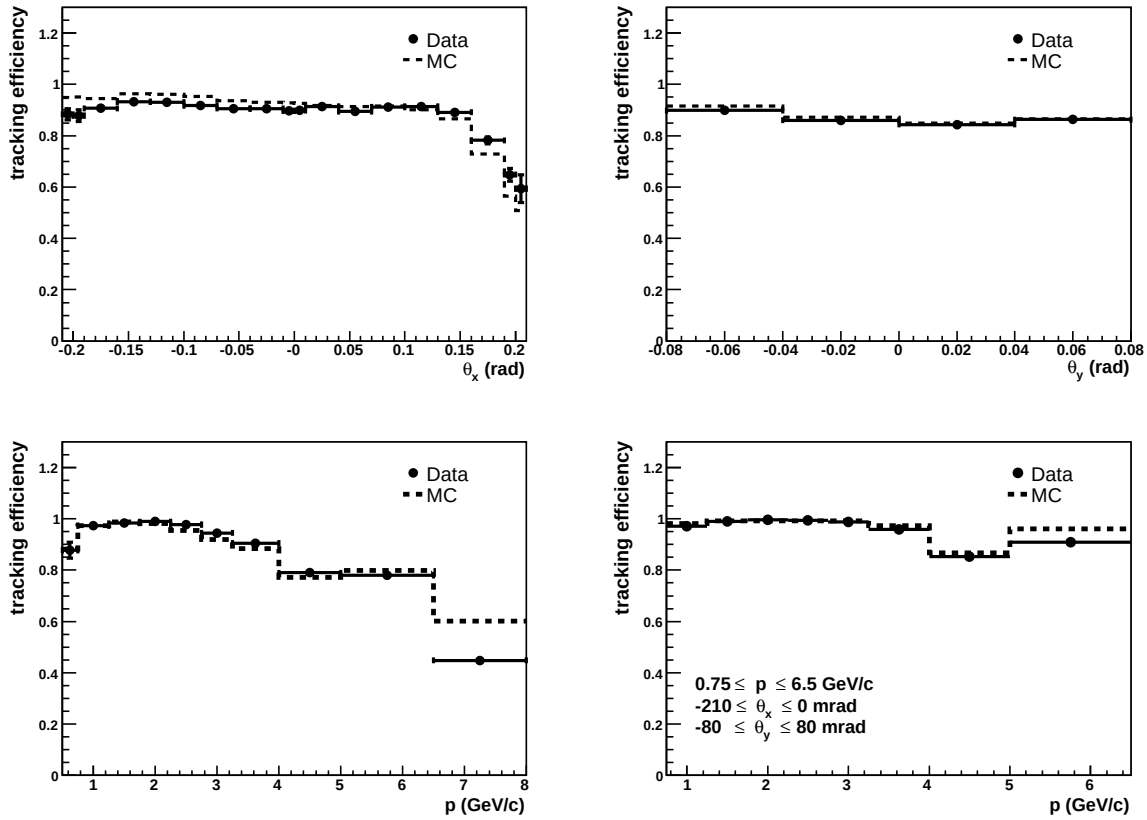

Figure 13: Upstream tracking efficiency as a function of kinematic variables, p, θ_x, and θ_y, at production for positively charged particles emanating from the vertex. Upper-left panel: As a function of θ_x. Upper-right panel: As a function of θ_y. Lower-left panel: As a function of p. Lower-right panel: As a function of p averaged over the θ_x and θ_y regions used in the present analysis only. The efficiency is close to 100% for negative θ_x and momenta less than 4 GeV/c, and drops for high values of θ_x (due to the dipole's acceptance) and for high momenta (due to a weakness in the reconstruction algorithm, see text). Points with error bars correspond to data, the dashed line to Monte Carlo. The agreement is excellent, except in the momentum bin 6.5 GeV/$c \leq p <$ 8.0 GeV/c, where there is a 25% difference. This bin is not used in the analysis (see text).

limitation imposed by the dipole magnet, as clearly demonstrated by Fig. 13 (upper-right), which shows a flat distribution in the non-bending plane θ_y and Fig. 13 (lower-left), which shows the efficiency as a function of p, integrated for all θ_x. The drop of the efficiency for large values of θ_x is fully correlated with the drop at low p. This can be seen in Fig. 13 (lower-right), where the reconstruction efficiency as a function of p for negative θ_x (particles fully contained in the dipole acceptance) is shown. The efficiency is flat and close to 100% up to 4 GeV/c, and drops for the last two bins. The efficiency as a function of θ_x (θ_y) for momenta less than 4 GeV/c is close to 100%, indicating that the loss of efficiency is due to the efficiency drop at $p >$ 4 GeV/c. The efficiency of the momentum reconstruction algorithm is lower near the edge of the acceptance because it requires a number of trajectories around the best fit to be inside the aperture. This requirement reflects in a drop of overall efficiency for $\theta_x >$ 150 mrad.

The drop in reconstruction efficiency at high momenta is due to the lack of optimization, at high momentum, of the reconstruction algorithm. Its effect on the calculation of the cross-section is very small (in practice it translates into a slightly larger error in the higher momentum bins, which are dominated by statistical errors). Except for the highest-momentum bin, the data are well described by the Monte Carlo.

4.5 Total reconstruction efficiency

The total tracking efficiency, $\varepsilon^{\rm track}$, can be expressed as the product of two factors. One factor represents the downstream (of the dipole magnet) tracking efficiency and the other represents the efficiency for matching a downstream segment to a vertex (for tracks originating inside the target volume):

$$\varepsilon^{\rm track} = \frac{N^{\rm down}}{N^{\rm parts}} \cdot \frac{N^{\rm vertex2}}{N^{\rm down}} = \varepsilon^{\rm down} \cdot \varepsilon^{\rm vertex2} \ , \tag{4}$$

where $N^{\rm vertex2}$ is the number of VERTEX2 tracks, which corresponds to $N^{\rm track}$ in Eq. 1. In the momentum range of interest for this analysis, a good time-of-flight measurement is essential for particle identification. Therefore, one also requires a good TOFW hit matched to the track. In addition to selecting the scintillator slab hit by the particle, this matching consists of a cut in the matching χ^2 of the track with the TOFW hit coordinate that is measured by the time difference of the signals at the two sides of the scintillators.

The TOFW hit matching efficiency was computed using the same track sample as in the previous section:

$$\varepsilon^{\rm ToF} = \frac{N^{\rm ToF}(\exists{\rm ToF}; \exists p_4, r_{\rm V4} \leq 30 \text{ mm}, \chi^2_{\rm match} \leq 10)}{N^{\rm vertex4}(\exists p_4, r_{\rm V4} \leq 30 \text{ mm}, \chi^2_{\rm match} \leq 10)} \ , \tag{5}$$

where the condition $\exists$ToF guarantees that a TOFW hit was associated with the track, and the total reconstruction efficiency is found from:

$$\varepsilon^{\rm recon} = \varepsilon^{\rm track} \cdot \varepsilon^{\rm ToF} \ . \tag{6}$$

The total reconstruction efficiency is shown in Fig. 14. The inclusion of the TOF wall enhances the momentum-dependent acceptance cut (due to the fact that the TOF wall has a smaller geometrical acceptance than the NDC back-plane). The total reconstruction efficiency as a function of θ_x has a slight slope and drops for positive θ_x above 100 mrad. The total reconstruction efficiency as a function of p for negative θ_x is flat (and about 90%) for momenta below 4 GeV/c. The drop to 90% is due to the inefficiency in matching tracks to a TOFW hit. The agreement between data and Monte Carlo for the total reconstruction efficiency is excellent, except in the last momentum bin, where there is a 25% difference, reflecting the same effect already observed in the upstream efficiency.

5 Particle identification

A set of efficient PID algorithms to select pions and reject other particles is required for the current analysis. A Monte Carlo prediction of the differential yields of the various particle types shows that the pion production cross-section is small above 6.5 GeV/c, which is set as the upper limit of this analysis. The electron distribution peaks at low energy, while the proton background increases with momentum. The kaon yield is expected to be only a small fraction of the pion yield. In the momentum and angular range covered by the present measurements the proton yield is of a similar order of magnitude as the pion yield.

The PID strategy is based on the expectation of the yields of different particle types predicted by the Monte Carlo, and also on the momentum regions covered by the available PID detectors. The time-of-flight measurement with the combination of BTOF and TOFW systems (referred to as the TOFW measurement in what follows) allows pion–kaon and pion–proton separation to be performed up to 3 GeV/c and beyond 5 GeV/c respectively. The Cherenkov is used for hadron-electron separation below 2.5 GeV/c and pion–proton/kaon separation above 2.5 GeV/c in conjunction with the TOFW. The ECAL is used only to separate hadrons from electrons below 2.5 GeV/c to study the Cherenkov performance.

As mentioned above, the electron(positron) background is concentrated at low momentum ($p < 2.5$ GeV/c). It can be suppressed to negligible level with an upper limit on the CHE signal, given the fact that electrons

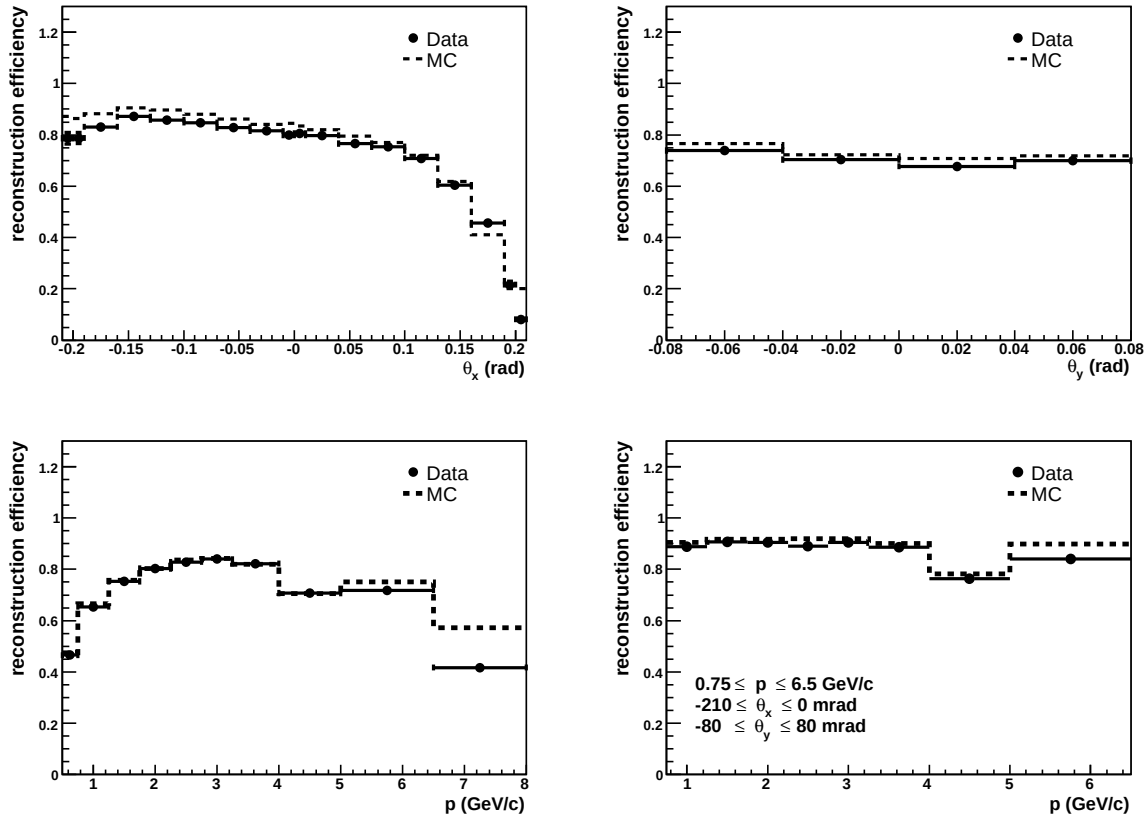

Figure 14: Total reconstruction efficiency as a function of kinematic variables, p, θ_x, and θ_y, at production for positively charged particles emanating from the vertex. Upper-left panel: as a function of θ_x. Upper-right panel: as a function of θ_y. Lower-left panel: as a function of p. Lower-right panel: as a function of p averaged over the θ_x and θ_y regions used in the present analysis only. The efficiency is close to 90% for negative θ_x and momenta less than 4 GeV/c, and drops for high values of θ_x (due to the TOFW acceptance) and for high momenta (due to a weakness in the reconstruction algorithm, see text). Points with error bars correspond to data, the dashed line to Monte Carlo. The agreement is excellent, except in the bin with highest momentum, where the difference is 6%.

are the only particles giving signal in the Cherenkov below the pion Cherenkov light emission threshold, which is equal to 2.6 GeV/c for the gas mixture used in HARP. In practice, any particle that has a momentum below 2.5 GeV/c and a signal in the CHE exceeding 15 photo-electrons is called an electron. In the following we will refer to this cut as the e-veto cut. The remaining electron background after the e-veto cut is negligible as studied in Ref. [14].

Having applied the e-veto cut to reject electrons and keeping in mind that there is a small fraction of kaons, one builds PID estimators for protons and pions by combining the information from TOFW and CHE using likelihood techniques (Sec. 5.2). Then, a cut on these PID estimators is applied to select pions or protons. The selected samples (raw pion and proton samples) will contain a small fraction of kaons, which can be estimated from the data, as described in Ref. [14]. This background is subtracted from the dominant yields of pions and protons.

The quantities that enter the cross-section calculation are the raw pion and proton yields and the PID efficiencies and purities (PID corrections) obtained by the application of the e-veto cut and cuts in the PID estimators. The PID corrections include the e-veto efficiencies, the kaon subtraction corrections and the pion-proton efficiency matrix (M^{id}, described in Sec. 6.4). A precise knowledge of these quantities (as a function of momentum and angle) requires the understanding of the responses of different PID detectors to the particle types considered. This is studied in detail using the data, taking advantage of the redundancy between the PID detectors.

These steps are explained briefly in the following sections. More details are given in Ref. [14].

5.1 Response of the PID detectors

The TOFW–CHE Probability Density Function (PDF), $P(\beta, N_{\rm phe}|i, p, \theta)$, describes the probability that a particle of type i (pion or proton) with momentum p and polar angle θ results in simultaneous measurements β in TOFW and $N_{\rm phe}$ in CHE. The latter comes directly from the calibrated CHE signal, while β is the particle velocity, computed as $\beta = l_{\rm tof}/(t_{\rm tof} \cdot c)$, where $l_{\rm tof}$ is the track length measured from the nominal vertex position to the TOFW hit position, $t_{\rm tof}$ is the measured time-of-flight and c is the speed of light. Assuming that the PID from both detectors are independent[1] the TOFW–CHE PDFs can be factorized in independent TOFW and CHE PDFs, such that $P(\beta, N_{\rm phe}|i, p, \theta) = P(\beta|i, p, \theta) \cdot P(N_{\rm phe}|i, p, \theta)$.

5.1.1 TOFW response

The use of the particle velocity, β, to characterize the TOFW response has several advantages. Its distribution is nearly Gaussian–the agreement between data and Monte Carlo is sufficient for the current analysis–and it discriminates very effectively between pions and protons up to momenta around 5 GeV/c (at this energy the separation between the average values of the proton and pion Gaussians is around 2.2σ). These points are illustrated in Fig. 15.

To build the TOFW PDFs one should know the β distribution of pions and protons as a function of the particle momentum and angle. In order to maximize the efficiency of the selection algorithm and to avoid any possible bias in the PID corrections related with a data–MC disagreement, those distributions have been measured from the data. This requires the ability to select pure and unbiased samples of pions and protons from the data. Samples of pions with negligible contamination from other species can be obtained selecting particles of negative charge passing the e-veto cut (Fig. 16, left panel). At low momentum, the proton parameters can be obtained by simply fitting to a Gaussian the proton part of the β distribution, since this is well separated from pions (Fig. 16, central panel). At large momentum (> 2.5 GeV/c), the proton and pion distributions overlap significantly. In this case, pions are rejected to the 1% level by a cut on the CHE signal (Sec. 5.1.2). The resulting sample contains a majority of protons and residual contaminations from pions and kaons. In this momentum range the proton parameters can be obtained

[1] The use of the reconstructed momentum instead of the true momentum in the probability density function $P(\beta, N_{\rm phe}|i, p, \theta)$ introduces a small correlation between TOFW and CHE. However, the good momentum resolution of the forward spectrometer ($\sigma_p/p < 10\%$) makes this correlation very small. At the level of precision required by this analysis this effect can be neglected.

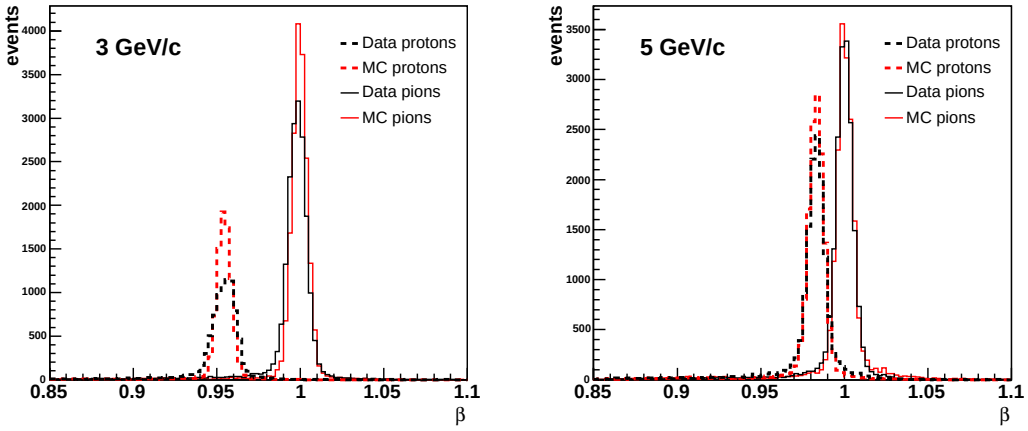

Figure 15: The distribution of the particle velocity, β, for pions and protons of 3 and 5 GeV/c, for both data (corresponding to a sample of beam particles, selected as pions or protons by the beam instrumentation) and its corresponding Monte Carlo simulation. At 3 GeV/c the separation between the two populations is $\approx 5\sigma$, and the separation is still $\approx 2.2\sigma$ at 5 GeV/c. The proton and pion peaks in the Monte Carlo have been separately normalized to the area of the corresponding peaks in the data.

by fitting the inclusive β distribution to a triple Gaussian with fixed pion and kaon shapes[2], as shown in the right panel of Fig. 16. A full description of this technique is given in Ref. [14].

Figure 17 shows the mean value and the standard deviation of β for pions and protons. The left panel of Fig. 17 shows the comparison between the values obtained with the method explained above and the ones obtained using the MC information about the true particle type. In both cases, the same sample of Monte Carlo data has been used. The observed good agreement confirms that the proposed technique does not bias the pion and proton parameters. The result of the application of this method to the data is shown in the right panel of Fig. 17. This plot also shows the comparison between data and Monte Carlo when using the same method for the selection of pure particle samples. We observe a global shift of about 0.003 in β which can be attributed either to a TOFW misalignment of 3 cm along the z direction or to a time offset of 0.1 ns between the TOFW and the BTOF system. In order to account for this difference the analysis uses the PDFs based on the β distribution measured in the data directly when treating 'data-events' and the PDFs based on the Monte Carlo distribution when treating 'Monte Carlo events'. The TOFW PDFs are parametrized as the sum of a dominant Gaussian function and a term accounting for non-Gaussian outliers, normalized to the observed effect.

5.1.2 Cherenkov response

The Cherenkov detector is used digitally in this analysis: a signal is accepted if the number of photoelectrons is larger than 2. To obtain the CHE PDFs for a given momentum and angular bin, the fraction of true pions (protons) with negative (positive) signal in the CHE is measured. The number of true particles of a given type is obtained with a technique similar to the one used for the TOFW detector, in this case by applying a strict cut to the TOFW measurement (see Ref. [14] for the details). Fig. 18 (left panel) shows the CHE inefficiency for particles of negative charge (essentially pions) as a function of the reconstructed momentum and angle. The asymptotic inefficiency for pions, *i.e.* above a momentum of 3.5 GeV/c, is estimated to be $(1.0 \pm 0.5)\%$.

In the momentum range studied no signal is expected in the CHE for protons. However, in a fraction of events, the reconstruction algorithm wrongly associates the CHE hit from a pion or an electron to the

[2]The pion shape is obtained from the data, while the kaon shape is calculated using the MC information.

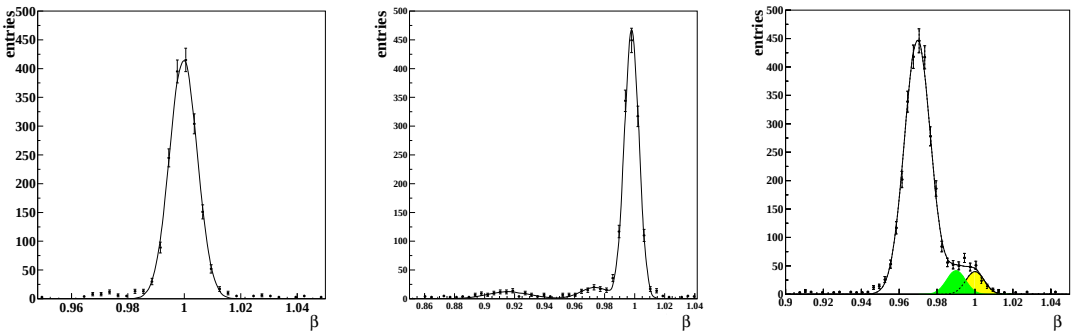

Figure 16: Inclusive β distribution for pions, kaons and protons passing the e-veto cut. Left panel: negative particles (essentially pions) with reconstructed momentum between 3.25 and 4 GeV/c. Central panel: positive particles with reconstructed momentum between 1.75 and 2.25 GeV/c. Right panel: positive particles (mostly protons) with reconstructed momentum between 3.25 and 4 GeV/c. In the right panel, the kaon and pion Gaussians are also shown (shaded areas).

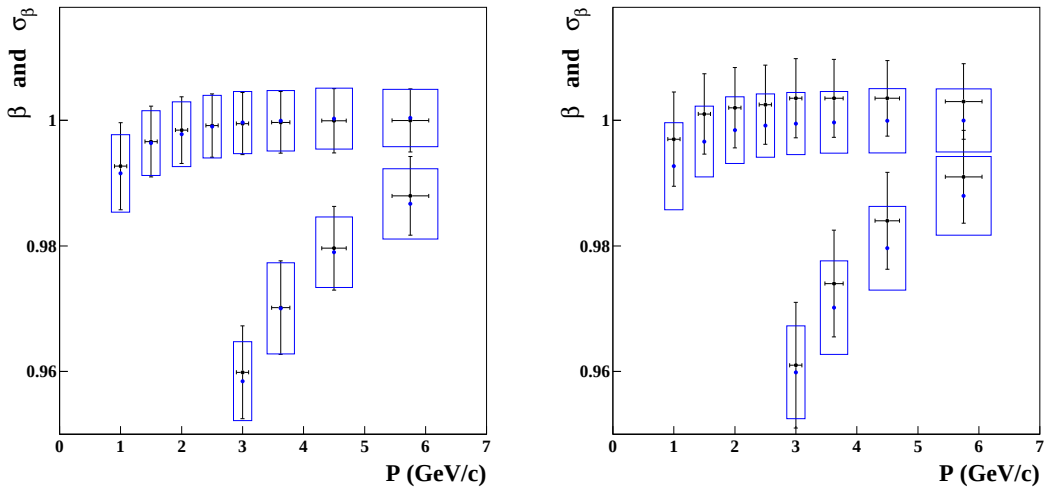

Figure 17: Mean value of β (points) and its standard deviation (error bars and rectangles) as a function of momentum for protons and pions. On the left, MC events only, obtained using only reconstructed quantities to select pure samples (points with error bars) and using the MC information about the true particle type (rectangles). On the right, points with error bars correspond to similarly selected events from real data, and the rectangles correspond to equivalent MC events. The centres of the rectangles are indicated with points.

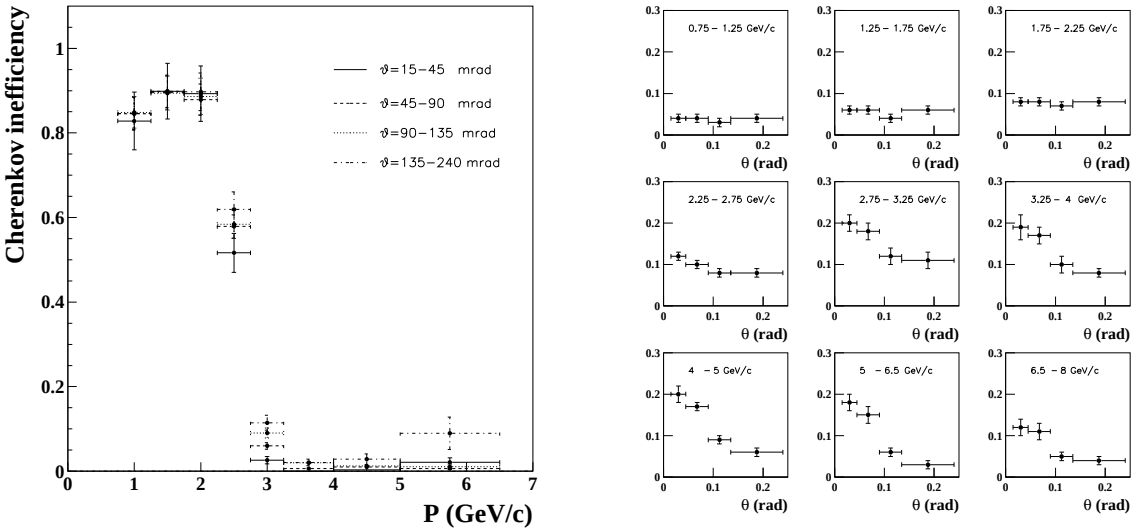

Figure 18: Left panel: CHE pion inefficiency as a function of the momentum for different angular regions. Right panel: CHE proton efficiency as a function of the angle for different momentum regions.

proton and consequently, a fraction of protons has a non-negligible amount of associated photoelectrons. This is a potential source of background (as well as of pion inefficiency), particularly important at high momentum, where the TOFW is not applicable. The efficiency of the CHE for protons has been measured as a function of momentum and angle. The results are shown in Fig. 18 (right panel). This non-zero efficiency is fully taken into account in this analysis as explained in Ref. [14]. The CHE PDFs are given in Fig. 18.

5.2 The pion-proton PID estimators

The assignment of a particle type $i = \pi, \mathrm{p}$ to a reconstructed track is based on a cut $P_i > P_{\mathrm{cut}}$ in a PID estimator P_i, the so-called combined PID probability, which is built by using Bayes' theorem:

$$P_i = P(i|\beta, N_{\mathrm{phe}}, p, \theta) = \frac{P(\beta, N_{\mathrm{phe}}|i, p, \theta) \cdot P(i, p, \theta)}{P(\beta, N_{\mathrm{phe}}|\pi, p, \theta) \cdot P(\pi, p, \theta) + P(\beta, N_{\mathrm{phe}}|\mathrm{p}, p, \theta) \cdot P(\mathrm{p}, p, \theta)} \ , \tag{7}$$

where $P(\beta, N_{\mathrm{phe}}|i, p, \theta)$ are the TOFW–CHE PDFs described above, and $P(i, p, \theta)$ is the prior, describing the a priori probability that a particle passing the event and track selection criteria (Secs. 6.1 and 6.2) is of type i and has momentum p and polar angle θ.

Several simplifications have been made to the general formula (7). They result in a slightly less efficient particle type selection, which implies a larger error on the PID corrections. However, the additional error is negligible when added in quadrature to the dominant non-PID errors. As a first approximation, the PDFs that enter the PID estimator were averaged over all angles. As second approximation, equally probable priors were used, so that they cancel. In this case only the information from the current track is used to build the PID estimator. The PID estimator built with no priors does not have a full probabilistic meaning and cannot be used directly to estimate the particle yields. Instead, the raw pion and proton yields must be corrected by the efficiencies and purities obtained by the application of the cut $P_i > P_{\mathrm{cut}}$, as will be described in Sec. 7.5. Finally, the TOFW–CHE PDFs can be factorized in independent TOFW and CHE PDFs, as explained before. The final PID estimator is then represented by the formula:

$$P_i = P(i|\beta, N_{\mathrm{phe}}, p) = \frac{P(\beta|i, p) \cdot P(N_{\mathrm{phe}}|i, p)}{P(\beta|\pi, p) \cdot P(N_{\mathrm{phe}}|\pi, p) + P(\beta|\mathrm{p}, p) \cdot P(N_{\mathrm{phe}}|\mathrm{p}, p)} \ . \tag{8}$$

6 Calculation of the cross-section

The double-differential cross-section for the production of a particle of type α can be expressed in the laboratory system as:

$$\frac{d^2\sigma_\alpha}{dp_i d\theta_j} = \frac{1}{N_{\rm pot}} \frac{A}{N_A \rho t} M^{-1}_{ij\alpha i'j'\alpha'} \cdot N^{\alpha'}_{i'j'} \ , \tag{9}$$

where $\frac{d^2\sigma_\alpha}{dp_i d\theta_j}$ is expressed in bins of true momentum (p_i), angle (θ_j) and particle type (α), and the terms on the right-hand side of the equation are:

- $N^{\alpha'}_{i'j'}$ is the number of particles of observed type α' in bins of reconstructed momentum ($p_{i'}$) and angle ($\theta_{j'}$). These particles must satisfy the event, track and PID selection criteria, explained below. This is the so called 'raw yield'.
- $M^{-1}_{ij\alpha i'j'\alpha'}$ is a correction matrix which corrects for finite efficiency and resolution of the detector. It unfolds the true variables $ij\alpha$ from the reconstructed variables $i'j'\alpha'$ and corrects the observed number of particles to take into account effects such as reconstruction efficiency, acceptance, absorption, pion decay, tertiary production, PID efficiency and PID misidentification rate.
- $\frac{A}{N_A \rho t}$ is the inverse of the number of target nuclei per unit area (A is the atomic mass, N_A is the Avogadro number, ρ and t are the target density and thickness).
- $N_{\rm pot}$ is the number of incident protons on target.

The summation over reconstructed indices $i'j'\alpha'$ is implied in the equation. It should be noted that the experimental procedure bins the result initially in terms of the angular variable θ, while the final result will be expressed in terms of the solid angle Ω. Since the background from misidentified protons in the pion sample is not negligible, the pion and proton raw yields ($N^{\alpha'}_{i'j'}$, for $\alpha' = \pi, {\rm p}$) have to be measured simultaneously.

For practical reasons, the background due to interactions of the primary proton outside the target (called 'Empty target background') has been taken out of the correction matrix M^{-1}. Instead, a subtraction term is introduced in Eq. 9:

$$\frac{d^2\sigma_\alpha}{dp_i d\theta_j} = \frac{1}{N_{\rm pot}} \frac{A}{N_A \rho t} M^{-1}_{ij\alpha i'j'\alpha'} \cdot \left[N^{\alpha'}_{i'j'}({\rm T}) - N^{\alpha'}_{i'j'}({\rm E}) \right] \ , \tag{10}$$

where (T) refers to the data taken with the aluminium target and (E) refers to the data taken with no target (Empty target).

The event, track and particle identification selection criteria will be described first, then the method used to obtain the cross-section and each of the corrections will be described in more detail.

6.1 Event Selection

In the 12.9 GeV/c beam protons are selected by vetoing particles which give a signal in any of the beam Cherenkov detectors. Only particles which give a good timing signal in all three beam timing detectors, leave a single track in the MWPCs, and are not seen in the halo detectors are accepted. A good timing measurement is defined as a set of three hits, one in each of the timing detectors, with their relative time difference consistent with a beam particle. The distribution of the position of beam particles extrapolated to the target is shown in Fig. 19 (left panel). The size of the target is indicated by a circle. Only particles extrapolated within a radius of 10 mm are accepted. By evaluating the number of tracks reconstructed in the spectrometer as a function of the extrapolated impact point of the MWPC track to the target, it

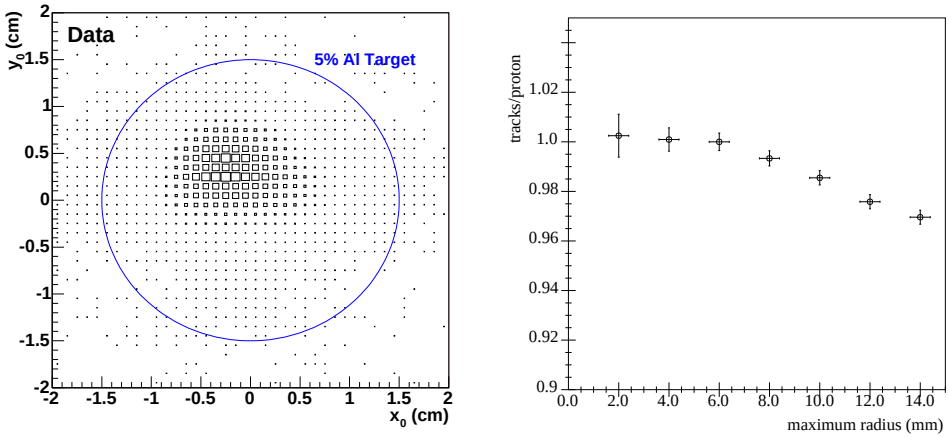

Figure 19: Left panel: reconstructed position (x_0, y_0) of beam particles at the reference z_0 plane of the target. The circle gives the position and size of the target. Right panel: observed number of tracks per incident proton as a function of the maximum accepted measured radius of incidence of the beam track. The ratio is normalized to unity at 6 mm.

Data Set	**Al 5% 12.9 GeV/c**	**12.9 GeV/c Empty Target**
Protons on target	17,954,688	4,769,408
Total events processed	4,710,609	771,330
Events with accepted beam proton	3,404,372	547,838
Prescaled triggers with accepted beam proton	280,542	74,522
FTP triggers	2,087,732	225,639
FTP trigger rate = (FTP triggers / pot)	0.116	0.047
Total good tracks	209,929	11,704

Table 1: Total number of events in the 12.9 GeV/c aluminium 5% $\lambda_{\rm I}$ target and empty target data sets, and the number of protons on target as calculated from the prescaled trigger count.

was determined that $(1.5 \pm 0.5)\%$ of the proton tracks selected according to these criteria miss the target, as shown in Fig. 19 (right panel). A correction for this loss has been applied. The MWPC track was required to have a measured direction within 5 mrad of the nominal beam direction to further reduce halo particles. The purity of this proton sample is estimated to be better than 99.5%.

Prior to those cuts, the beam particle was required to satisfy the trigger conditions described in Section 2.1. Applying the above selection cuts to the 12.9 GeV/c aluminium 5% $\lambda_{\rm I}$ target data set and the 12.9 GeV/c empty target data set results in the total statistics listed in Table 1. The total number of protons on target (N_{pot} in Eq. 9) listed in the table is exactly the number to be used in the overall normalization of the cross-section results, and is known to better than 1%. The total number of protons on target is counted using prescaled 'beam' triggers that were continuously recorded at the time of data taking. The trigger condition for the prescaled beam triggers only involved a simple coincidence of scintillators in the beam line with no requirement of an interaction in the target. Using subsamples of the triggers the prescale factor was checked to confirm it had its preset value 1/64. Because the selection criteria for beam protons used in event analysis and prescaled beam proton events are the same, the efficiencies for these cuts cancel, and the total normalization can be known without additional systematic uncertainty.

Events to be used in the analysis must also contain one or more hits in the forward trigger plane (FTP).

6.2 Track Selection

The recorded events have been processed according to the track selection criteria listed below:

- The VERTEX2 track momentum is measured (see Section 3.2).
- A track segment in NDC2 or in the back-plane is used in track reconstruction.
- Number of hits in a road around the track in NDC1 ≥ 4 (this is applied to reduce non-target interaction backgrounds).
- The average χ^2 for hits with respect to the track in NDC1 ≤ 30,
- Number of hits in the road around the track in NDC2 ≥ 6 (this is applied to reduce background of tracks not coming from the target).
- The track has a matched TOFW hit.

The result of applying these cuts to the entire 12.9 GeV/c aluminium 5% $\lambda_{\rm I}$ and empty target data sets is listed in Table 1.

In addition, geometrical cuts are applied. As described in Sec. 4 for positive θ_x the efficiency is momentum dependent. This region is avoided in the analysis by defining the fiducial volume as $-210 \leq \theta_x < 0$ mrad (thus, only particles in the negative half of the bending plane of the dipole are accepted) and $-80 < \theta_y < 80$ mrad. The restricted acceptance in θ_y is imposed to avoid edge effects of the dipole, possible fringe effects in the magnetic field, etc. Since the behaviour of the spectrometer is calibrated with beam particles (at $\theta_y = 0$) the analysis restricts θ_y to a rather small region around the horizontal mid-plane of the spectrometer. In order to avoid a correction for the acceptance of the FTP-trigger and to avoid background from beam protons, cross-sections are given for $\theta > 30$ mrad.

6.3 PID selection

Particle identification criteria (described in Sec. 5) are applied to the tracks passing the event and track selection criteria. First the e-veto cut is applied to reject electrons and then a cut in the PID estimator is applied to distinguish between pions and protons. Figure 20 shows the combined pion probability (PID estimator for pions) for positive particles passing the e-veto cut. A large population of particles in the low probability region is attributed to a contribution from protons. The small peaks at 0.5 correspond to particles which leave no useful information in either the TOFW or the Cherenkov. The peak near 0.9 in the right panel corresponds to particles which leave no useful information in the TOFW (presumably being non-Gaussian outliers) but which give a positive signal in the CHE.

It is found that the optimal cut to select pions with high efficiency and purity is $P_\pi > 0.6$. The cut is set at a value of probability where the track population is low, and thus the result is not sensitive to small changes in the exact value. Protons are selected by the condition $P_\pi < 0.4$ (equivalent to $P_{\rm p} > 0.6$).

6.4 The Atlantic and UFO analyses

Two complementary analyses have been performed with the aim of checking internal consistency, and checking for possible biases in the respective procedures. The first, called Atlantic[3], simplifies the problem of unfolding by decomposing the correction matrix of Eq. (9) into distinct independent contributions, which are computed mostly using the data themselves. The second analysis, called UFO (from UnFOlding), performs a simultaneous unfolding of p, θ and PID, with a correction matrix M^{-1} computed mainly using the Monte Carlo.

[3] 'Atlantic' for Analysis of Tracks at Low ANgle with Tof Id and Cherenkov id

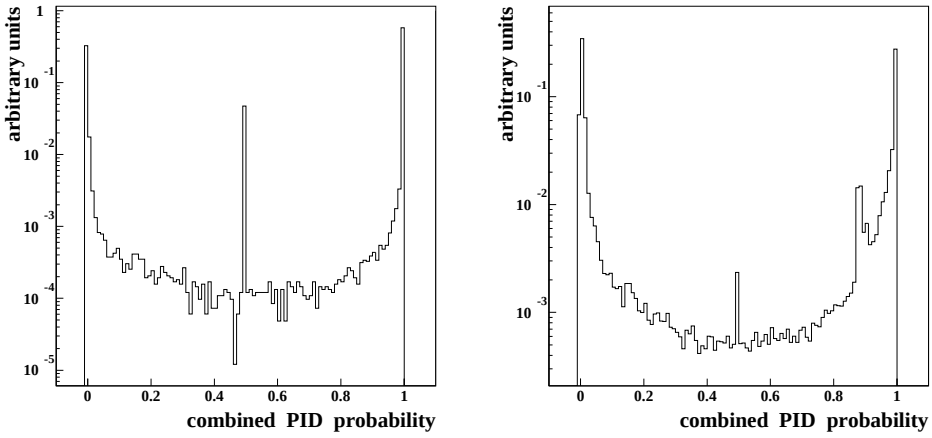

Figure 20: Combined pion probability (logarithmic scale) for positive particles passing the e-veto cut. The left panel shows positive particles below CHE threshold. The right panel shows positive particles above CHE threshold. The meaning of the different spikes is explained in the text.

The UFO procedure uses an iterative Bayesian technique, described in Ref. [15], in order to unfold the measured distribution. The central assumption of the method is that the probability density function in the physical parameters ('physical distribution') can be approximated by a histogram with bins of sufficiently small width. A population in the physical distribution of events in a given cell $ij\alpha$ generates a distribution in the measured variables, $M_{ij\alpha i'j'\alpha'}$, where the indices $ij\alpha$ indicate the binning in the physical angular, momentum and PID variables, respectively, and $i'j'\alpha'$ the binning in the measured variables. Thus the observed distribution in the measurements can be represented by a linear superposition of such populations. The task of the unfolding procedure consists then in finding the number of events in the physical bins for which the predicted superposition in the measurement space gives the best description of the data.

In order to predict the population of the migration matrix element $M_{ij\alpha i'j'\alpha'}$, the resolution, efficiency and acceptance of the detector are obtained from the Monte Carlo. This is a reasonable approach, since the Monte Carlo simulation describes most of these quantities correctly (see Section 4). Where some deviations from the control samples measured from the data are found, the data are used to introduce (small) corrections to the Monte Carlo.

Although some corrections are common to both approaches, large differences between the results of these two analyses would indicate inconsistencies in the simplifications adopted by Atlantic for unfolding, the hypothesis of correct Monte Carlo description of the detector on which UFO is based, or both. As it turns out, the analyses are consistent within the overall systematic error, reinforcing our confidence in the correctness of the results presented here. For clarity, in the rest of this paper only the Atlantic analysis will be discussed.

7 The Atlantic analysis

As discussed in section 3.2, both the momentum and angular resolution are small compared with the binning of the cross-section. Migration effects are, therefore, small. In particular, angular migration can be neglected. In addition, kinematic migration is almost decoupled from pion–proton PID migration. As explained in Sec. 5 electron and kaon ID has been decoupled from the dominant pion–proton ID so that electron and kaon correction factors are diagonal in the PID variables. With the above considerations the correction matrix M^{-1} can be written as:

$$M^{-1}_{ij\alpha i'j'\alpha'} = (M^{id}_{ij;\alpha\alpha'})^{-1} \cdot \varepsilon^{-1}_{ij\alpha'} \cdot (M^{\theta}_{jj'})^{-1} \cdot (M^{p}_{ii'})^{-1} \ , \tag{11}$$

where again reconstructed indices are indicated with a prime. The corrections are applied in the order from right to left as they appear in the equation. The symbols in Eq. (11) have the following meaning:

$\varepsilon^{-1}_{ij\alpha'}$ is the collection of factors applying the corrections that are diagonal in the PID indices: reconstruction efficiency, acceptance, physical loss of particles (absorption, decay), background from tertiary interactions, e-veto efficiency and kaon subtraction;

$(M^{p}_{ii'})^{-1}$ is the simplified unfolding matrix correcting for the momentum smearing which only depends of the indices i and i' representing the true and reconstructed momentum bins, respectively;

$(M^{\theta}_{jj'})^{-1}$ is the identity matrix, representing the assumption that the smearing effect in the angular measurement is negligible; and

$(M^{id}_{ij;\alpha\alpha'})^{-1}$ is the matrix which corrects for pion–proton PID inefficiency and migration, which is diagonal in i, i' and j, j', but built of two–by–two sub-matrices, each different and non-diagonal in the PID variables α, α'.

The diagonal efficiency correction

$$\varepsilon^{-1}_{ij\alpha'} = w^{\text{recon}}_{ij} \cdot w^{\text{acc}}_{ij} \cdot w^{\text{absorption}}_{ij\alpha'} \cdot w^{\text{tertiaries}}_{ij\alpha'} \cdot \eta^{\text{K}}_{ij\alpha'} \cdot \eta^{\text{e}}_{ij\alpha'} \tag{12}$$

is composed of the following factors:

w^{recon}_{ij} the correction for the overall reconstruction efficiency;

w^{acc}_{ij} the correction for the acceptance;

$w^{\text{absorption}}_{ij\alpha'}$ the correction for the loss of particles due to absorption and decay;

$w^{\text{tertiaries}}_{ij\alpha'}$ the correction for the background of tertiary particles generated by the secondaries produced in the target;

$\eta^{\text{K}}_{ij\alpha'}$ is the factor correcting for the kaon background; and

$\eta^{\text{e}}_{ij\alpha'}$ is the factor correcting for the effects of the electron veto.

The first two corrections are the same for pions and protons while the latter four also depend on the particle type. It is worth noting that the efficiency correction is expressed in terms of the true momentum and angle, and in terms of the reconstructed particle type (α'). This is because these corrections are applied before PID unfolding, as explained below.

As advanced in Sec. 3.3, some of the above corrections are computed as a function of p, θ_x and θ_y, while some others are directly expressed in the final variables (p, θ). In the first case, the transformation to polar coordinates (p, θ) is done integrating over all θ_x and θ_y resulting in a given θ bin. In particular, the four first corrections of Eq. (12), denoted by w, are computed as a function of (p, θ_x, θ_y).

Each of the above corrections will be described in the sections below.

7.1 Reconstruction and acceptance corrections

The correction for the total reconstruction efficiency, requiring a momentum measured and a matched TOFW hit (computed in Sec. 4), is introduced as a weight $w^{\text{recon}}_{ij} = [\varepsilon^{\text{recon}}(p, \theta_x, \theta_y)]^{-1}$.

It is necessary to correct for the restricted definition of fiducial volume. Inside the θ_y acceptance (that is, below the vertical cutoff at $\theta_y = \pm 80$ mrad) the correction is a simple factor of 2 due to the fact that tracks with $\theta_x > 0$ are not used. For values of θ above the θ_y cutoff, the correction is:

$$\varepsilon^{\text{acc}}(p, \theta_x, \theta_y) = \frac{1}{\pi} \cdot \arcsin\left(\frac{\tan(\theta^{\text{cut}}_y)}{\tan(\theta)}\right) \ , \tag{13}$$

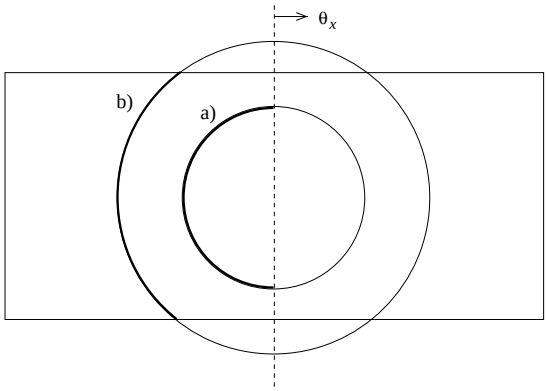

Figure 21: Sketch of the forward detector showing the two kinds of acceptance corrections, a) for $\theta < \theta_y^{\rm cut}$ where $\varepsilon^{\rm acc} = 0.5$, and b) for $\theta > \theta_y^{\rm cut}$ where $\varepsilon^{\rm acc}$ is given by Eq. (13).

describing the part of the circle which is inside the acceptance. Figure 21 shows a sketch depicting the two forms of geometrical acceptance and the origins of the correction factors listed above. The acceptance correction is then applied as a weight defined in Eq. (12), $w_{ij}^{\rm acc} = [\varepsilon^{\rm acc}(p, \theta_x, \theta_y)]^{-1}$. The above corrections are independent of the particle type.

7.2 Corrections for absorption, decay, and secondary interactions

An additional correction to consider is the absorption and decay of secondary pions (protons) in the materials of the detector components upstream of the magnet which prevent them from reaching the downstream region of the detector. These missing particles are not considered by the reconstruction efficiency described above. In some cases, *e.g.* pion decay, tertiaries are reconstructed as part of the original track. A correction is applied to take these cases into account. The overall absorption and decay rate is determined using the Monte Carlo, as a three-dimensional function $\varepsilon_\alpha^{\rm absorption}(p, \theta_x, \theta_y)$, whose projections are shown in Fig. 22. The overall effect is between 10% and 30% depending on p and θ_x. This effect is verified to be correct within 10% of its magnitude using beam particles. The 'absorption' correction is then applied as a weight introduced in Eq. (12), $w_{ij\alpha}^{\rm absorption} = [1 - \varepsilon_\alpha^{\rm absorption}(p, \theta_x, \theta_y)]^{-1}$ for both particle types separately.

A correction of opposite sign to the one above stems from positively charged particles which are not produced in the primary interaction between the incident proton and the target nucleus. These *tertiary particles* ('tertiaries') can come directly from the target (nuclear re-interactions, which is a small effect, since the target is only 5% $\lambda_{\rm I}$ in thickness) or from the region outside the target area. Another different background is due to particles produced by the interactions of the primary proton with material outside the target; this is corrected by taking data with empty target settings, and is described in Section 7.3. The correction for tertiaries is also computed with Monte Carlo, as a three-dimensional function $\varepsilon_\alpha^{\rm tertiaries}(p, \theta_x, \theta_y)$, shown in Fig. 23. The overall effect is between 2–3% (for pions) and 7% (for protons). In addition one needs to correct for pion decay resulting in muons which tend to be collinear with the original pion. The 'tertiary' correction is then applied as a weight introduced in Eq. (12), $w_{ij\alpha}^{\rm tertiaries} = 1 - \varepsilon_\alpha^{\rm tertiaries}(p, \theta_x, \theta_y)$. The correction is model-dependent, and has been assigned a systematic uncertainty of 100%.

The above corrections are computed separately for true pions and protons. However, for practical reasons, they are applied before PID unfolding assuming that they correspond to reconstructed pions and protons (hence the index α' in Eq. 12). The bias introduced by this approximation is negligible since pion–proton mixing is very small ($< 5\%$), as demonstrated in Fig. 26, and these corrections are either small ($< 7\%$ for tertiaries) or similar for both particle types (the absorption is similar while the decay of pions introduces a relatively small correction). Thus, the maximum bias would be of the order of 0.4%.

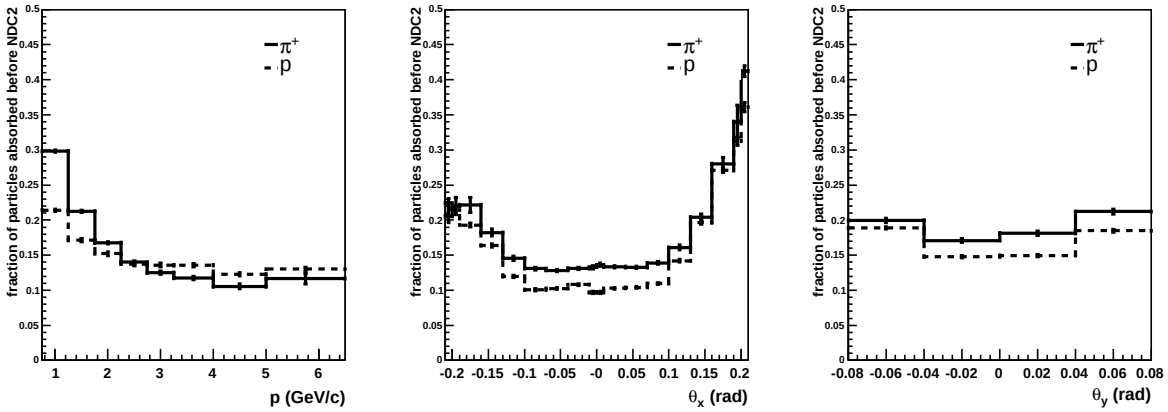

Figure 22: Absorption and decay rate as a function of kinematic variables, p, θ_x, and θ_y, at production for positively charged particles emanating from the vertex. Solid lines are pions, dashed lines are protons. Left panel: As a function of p. Central panel: as a function of θ_x. Right panel: As a function of θ_y. The acceptance effects for positive θ_x due to particles hitting the dipole walls are clearly visible. This effect is momentum dependent, as seen in the left panel.

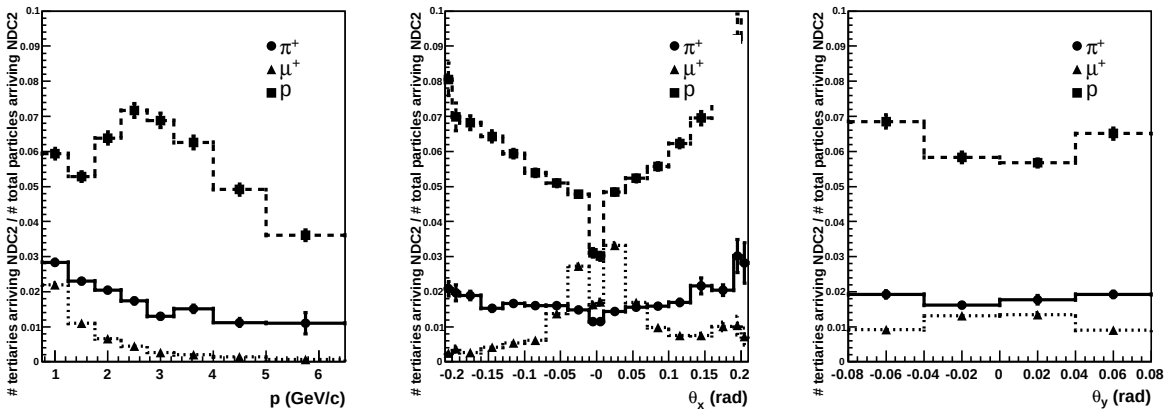

Figure 23: Tertiary particle rate as a function of kinematic variables, p, θ_x, and θ_y, at production for positively charged particles emanating from the vertex. Circles are pions, squares are protons, triangles are muons falsely identified as pions. Left panel: As a function of p. Central panel: as a function of θ_x. Right panel: As a function of θ_y.

7.3 Empty target subtraction

Several additional background sources need to be corrected for. The 'empty target' background is defined as the particles accepted by the selection criteria which are generated by interactions of the primary protons outside the target. The effect of this background is measured experimentally to a good approximation by taking data without placing the target in its holder.

The corrections described in the previous section are applied to both 5% λ_I target and empty target data sets. The empty target yield $N^{\alpha'}_{i'j'}(E)$ undergoes similar corrections to the yields measured with the target in place. The corrected empty target yields are then subtracted bin–by–bin from the corrected yields measured with target to remove this background. The relative normalization of the data with target and the empty target data is calculated using the number of protons on target accepted in the prescaled beam trigger. The overall subtraction is approximately 20% as shown in Fig. 24. The approximation used in this approach is to assume that the target itself does not influence the primary proton beam. To first order, this assumption introduces an error of 5% on the subtraction, given by the interaction length of the target.

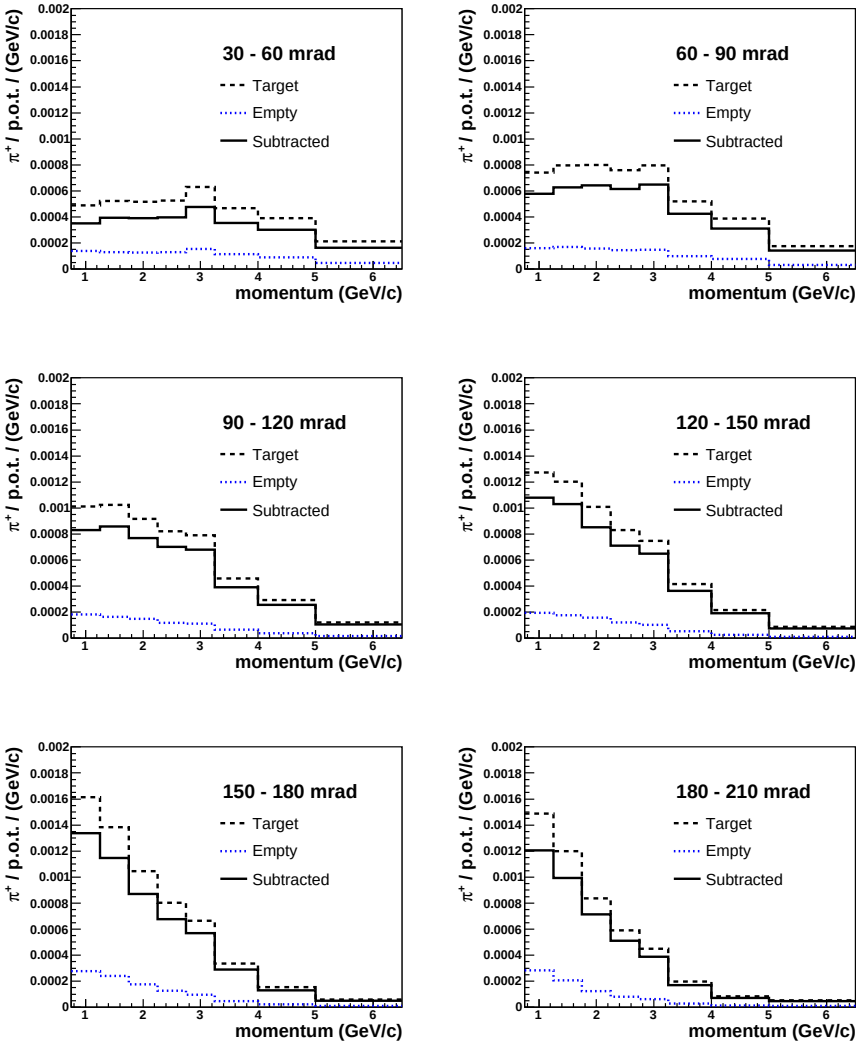

Figure 24: Positive pion yields, defined as pions per p.o.t (protons on target) as a function of momentum. Empty target yields are subtracted from target yields to remove backgrounds. The subtraction ranges from negligible to approximately 20%.

7.4 Corrections for electron-veto and kaon background

As discussed, the electron and kaon hypotheses are not considered by the PID selection algorithm. Kaons produced in the target and identified as either pions or protons have to be subtracted. Electrons are rejected by applying the CHE veto described above. This veto introduces a loss of efficiency for pions and protons. Multiplicative corrections are applied to the raw yields of pions and protons to compensate for these two effects as shown in Fig. 25.

The electron veto, described in Section 5, has some effect on pion and proton efficiency (around 7–10% of the pions and protons also give a signal in CHE below pion threshold, due to spatially associated electrons, *e.g.* the emission of hard δ-rays) which has been measured using both the Monte Carlo and the data (pure electron and hadron control samples were selected for that purpose using ECAL [14]). The weights $\eta^{\mathrm{e}}_{ij\alpha'}$ (Eq. (11)) are the inverse of the efficiencies for pions and protons to survive the electron veto requirement, respectively.

Kaons are subtracted from the raw yields of pions and protons. The kaon yield has being estimated from the data by fitting the inclusive TOFW-β distribution to the sum of three Gaussians (corresponding to protons, kaons and pions). An example is shown in Fig. 16. The kaon–to–pion and kaon–to–proton migration rates have also been determined from the data using the same technique as for pion–proton migration. The subtraction can be expressed as a correction factor $\eta^{\mathrm{K}}_{ij\alpha'}$, introduced in Eq. (11). The correction factors for pions and protons are shown in the bottom panels of Fig. 25. The correction for pions is only relevant ($\sim 3\%$) in the region of transition between TOFW and CHE ($\sim 3\,\mathrm{GeV}/c$), while the correction for protons is of the order of 10% in the entire phase space.

A detailed description of the methods used to determine the electron and kaon correction factors can be found in [14].

7.5 Unfolding the momentum dependence and the pion–proton yields

A yield of tracks with reconstructed momentum p_2 falling in a bin i' can be expressed as a superposition of tracks with true momentum in a bin i (p_i). The coefficients of this expansion are the elements of the momentum migration matrix of Eq. (11), $M^{p}_{ii'}$, that is $n(p_2)_{i'} = M^{p}_{ii'} \cdot n(p)_i$. To perform the momentum unfolding each observed track with measured quantities (p_2, θ_x, θ_y) populates several bins in a histogram of true variables (p, θ) with weights $M^{p}_{ii'}$. This is mathematically equivalent to the matrix inversion of Eq. (11).

The raw yield of identified pions and protons once corrected for all terms that are diagonal in the PID variables, $n^{\alpha'}_{ij} = \varepsilon^{-1}_{ij\alpha'} \cdot (M^{p}_{ii'})^{-1} \cdot (M^{\theta}_{jj'})^{-1} \cdot [N^{\alpha'}_{i'j'}(T) - N^{\alpha'}_{i'j'}(E)]$, is related to the true pion and proton yield, n^{α}_{ij}, by the PID migration matrix (also called PID efficiency matrix), $M^{id}_{ij;\alpha\alpha'}$, introduced in Sec. 6.4. In each bin of p and θ the matrix M^{id} is defined by:

$$\begin{pmatrix} n^{\pi'} \\ n^{\mathrm{p}'} \end{pmatrix} = \begin{pmatrix} M_{\pi\pi} & M_{\pi\mathrm{p}} \\ M_{\mathrm{p}\pi} & M_{\mathrm{pp}} \end{pmatrix} \cdot \begin{pmatrix} n^{\pi} \\ n^{\mathrm{p}} \end{pmatrix} , \tag{14}$$

where the elements of the matrix, in rows, are the fractions of observed pions that are true pions ($M_{\pi\pi}$), observed pions that are true protons ($M_{\pi\mathrm{p}}$), observed protons that are true pions ($M_{\mathrm{p}\pi}$), and observed protons that are true protons (M_{pp}). In this experiment this matrix can be computed using the redundancy in the data, as described in [14]. Figure 26 shows the elements of M^{id} (and the corresponding errors), as a function of momentum, for different angular intervals.

Then, the true yields can be computed by solving the system of linear equations given by Eq. (14). The covariance matrix of the true yield vector, n^{α}, is computed by error propagation, taking into account the covariance matrices of M^{id} and of the observed yield vector, $n^{\alpha'}$:

$$C[n^{\alpha}, n^{\beta}] = n^{\gamma'} \cdot C[(M^{id}_{\alpha\gamma'})^{-1}, (M^{id}_{\beta\delta'})^{-1}] \cdot n^{\delta'} + (M^{id}_{\alpha\gamma'})^{-1} \cdot C[n^{\gamma'}, n^{\delta'}] \cdot (M^{id}_{\beta\delta'})^{-1} ,$$

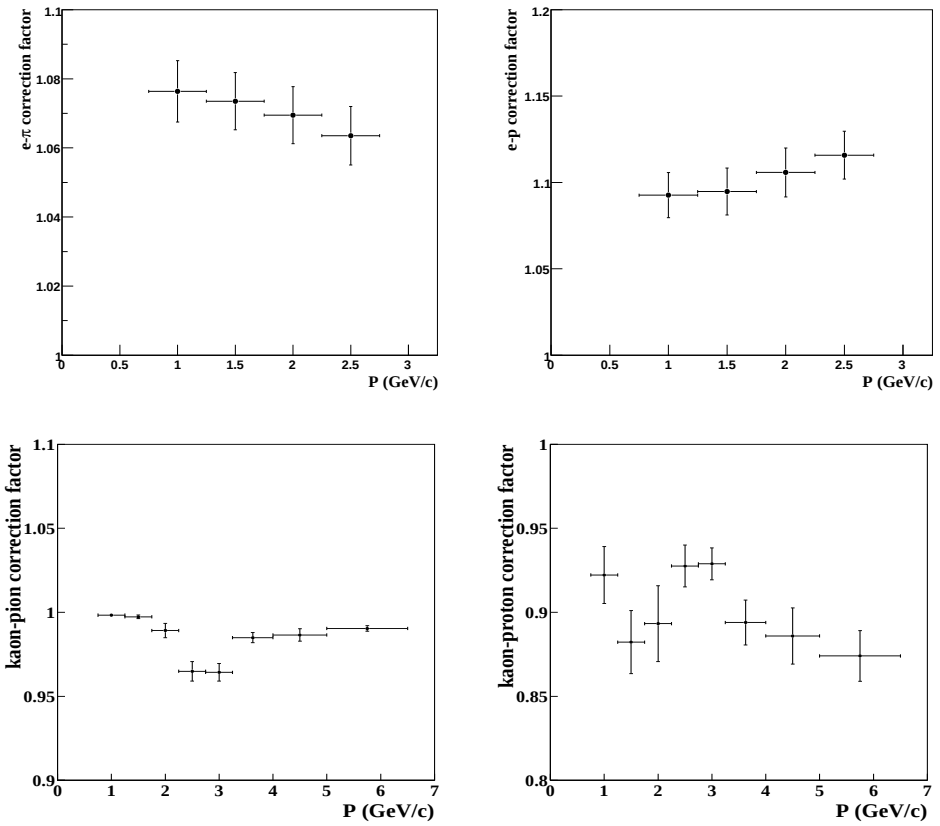

Figure 25: On the top, pion (left) and proton (right) e-veto correction factors averaged over angles. On the bottom the kaon-pion (left) and kaon-proton (right) correction factors in real data for $\theta = 90$ mrad.

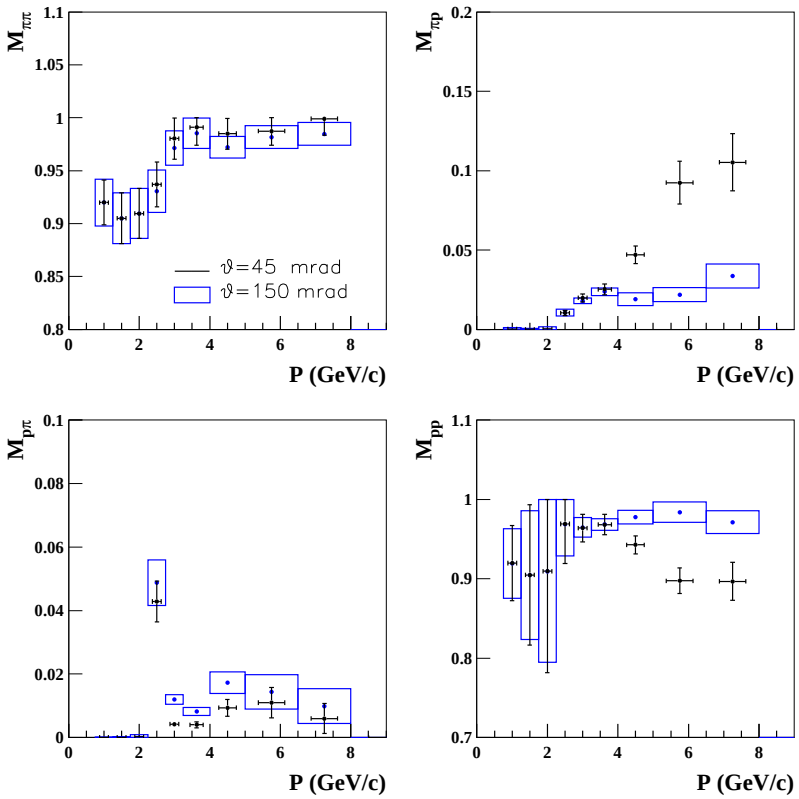

Figure 26: The elements of the PID efficiency matrix in the data, as a function of momentum, for two different angles. The probability cut is placed at 0.6.

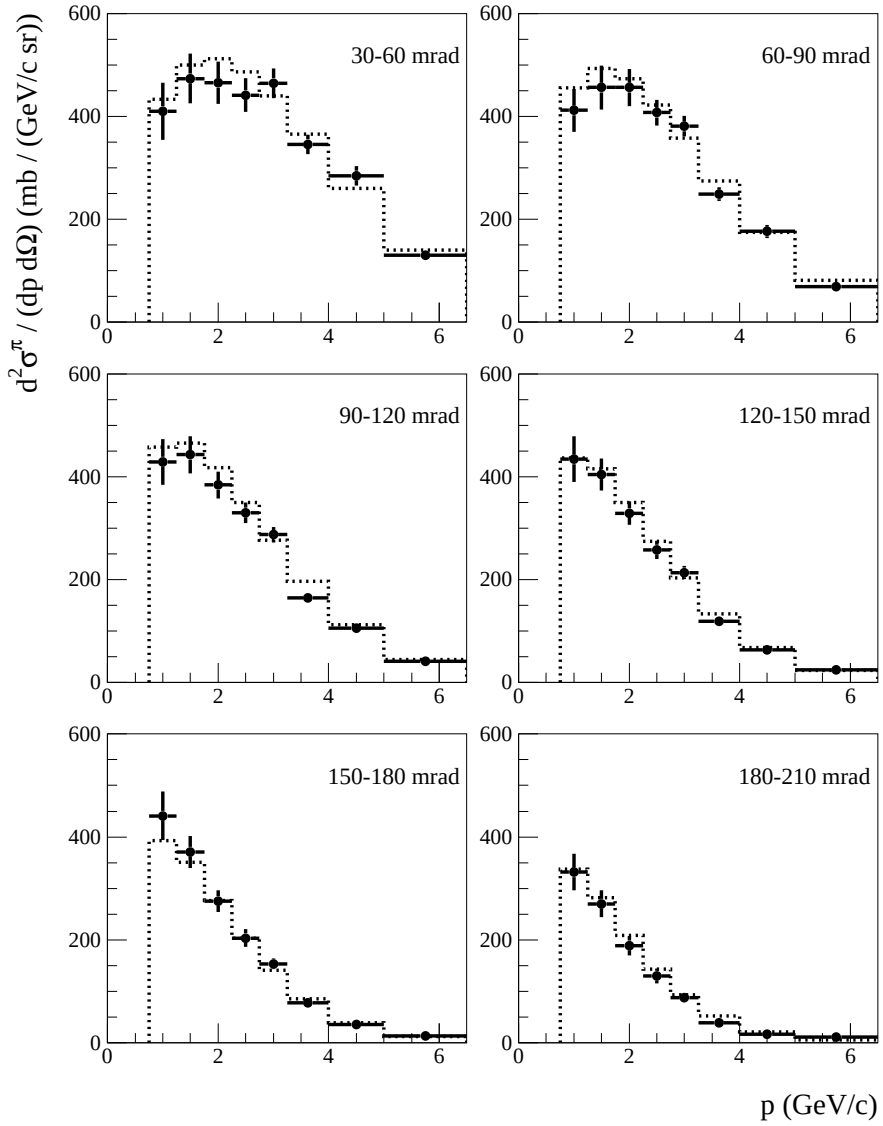

Figure 27: Measurement of the double-differential π^+ production cross-section in the laboratory system $d^2\sigma/(dpd\Omega)$ for incoming protons of 12.9 GeV/c on an aluminium target as a function of pion momentum p, in bins of pion polar angle θ. The data points are the measurements, the histogram represents the Sanford-Wang parametrization fitted to the data.

where all indices run over the pion and proton hypotheses.

8 Results

Figure 27 and Table 2 show the measurement of the double-differential cross-section for positive pion production in the laboratory system as a function of the momentum and the polar angle. Only diagonal errors are shown in the plots and table (a full discussion of the error evaluation is given below). Also shown in Figure 27 is a fit to a Sanford-Wang parametrization, which will also be discussed in this section.

$\theta_{\rm min}$ (mrad)	$\theta_{\rm max}$ (mrad)	$p_{\rm min}$ (GeV/c)	$p_{\rm max}$ (GeV/c)	$d^2\sigma^{\pi^+}/(dpd\Omega)$ (mb/(GeV/c sr))	
30	60	0.75	1.25	410 ±	56
		1.25	1.75	473 ±	49
		1.75	2.25	465 ±	41
		2.25	2.75	441 ±	33
		2.75	3.25	464 ±	29
		3.25	4.00	346 ±	18
		4.00	5.00	284 ±	18
		5.00	6.50	129.7 ±	8.1
60	90	0.75	1.25	412 ±	42
		1.25	1.75	456 ±	42
		1.75	2.25	456 ±	36
		2.25	2.75	407 ±	24
		2.75	3.25	381 ±	19
		3.25	4.00	249 ±	13
		4.00	5.00	176 ±	13
		5.00	6.50	68.9 ±	6.3
90	120	0.75	1.25	429 ±	45
		1.25	1.75	442 ±	36
		1.75	2.25	384 ±	26
		2.25	2.75	330 ±	20
		2.75	3.25	287 ±	15
		3.25	4.00	164.7 ±	9.8
		4.00	5.00	105.4 ±	8.1
		5.00	6.50	41.4 ±	4.3
120	150	0.75	1.25	434 ±	44
		1.25	1.75	404 ±	31
		1.75	2.25	329 ±	23
		2.25	2.75	258 ±	18
		2.75	3.25	213 ±	13
		3.25	4.00	119.1 ±	7.9
		4.00	5.00	62.8 ±	5.2
		5.00	6.50	24.2 ±	3.4
150	180	0.75	1.25	441 ±	47
		1.25	1.75	371 ±	31
		1.75	2.25	275 ±	21
		2.25	2.75	203 ±	17
		2.75	3.25	153 ±	10
		3.25	4.00	77.5 ±	7.1
		4.00	5.00	35.5 ±	4.5
		5.00	6.50	13.3 ±	1.7
180	210	0.75	1.25	332 ±	35
		1.25	1.75	270 ±	26
		1.75	2.25	189 ±	19
		2.25	2.75	130 ±	14
		2.75	3.25	87.8 ±	7.1
		3.25	4.00	38.3 ±	3.4
		4.00	5.00	16.6 ±	1.7
		5.00	6.50	10.4 ±	3.2

Table 2: HARP results for the double-differential π^+ production cross-section in the laboratory system, $d^2\sigma^{\pi^+}/(dpd\Omega)$. Each row refers to a different ($p_{\rm min} \leq p < p_{\rm max}, \theta_{\rm min} \leq \theta < \theta_{\rm max}$) bin, where p and θ are the pion momentum and polar angle, respectively. The central values quoted are the ones obtained via the Atlantic analysis discussed in the text. The square-root of the diagonal elements of the covariance matrix are also given.

8.1 Error estimates

A detailed error analysis has been performed to evaluate the accuracy of the pion cross-section measurement. The main errors entering in this measurement are listed below.

First, the statistical uncertainties associated with the track yields measured from the aluminium target setting and from the empty target setting (needed for subtraction, as explained above) have been included in the pion production cross-section uncertainty estimates.

Second, several uncertainties associated with the corrections needed to convert the measured track yields to true track yields have been evaluated. The track reconstruction efficiency correction is based on the combination of thin target aluminium and beryllium data sets. The main error associated with this computation is given by the size of the statistical sample. The correction to the pion and proton yields due to absorption or decay is computed via a Monte Carlo simulation. An uncertainty of 10% for both proton and pion yields has been assumed for this correction, in addition to the uncertainty due to the finite size of the simulated data sample used to estimate this correction. Similarly, simulated data (and their associated uncertainties) were used to estimate the correction for the contamination in the sample due to tertiary particles that are not produced in the target, but rather by the decay of secondaries, or by the interaction of secondaries in the spectrometer material. An uncertainty of 100% has been assumed for this subtraction, for both proton and pion yields. Furthermore, an uncertainty has been assigned to the empty target subtraction, in order to account for the effect of the target itself which attenuates the proton beam.

Third, uncertainties associated with the particle identification of tracks, and with the corrections needed to convert yields of tracks identified as pions to true pion yields, have been included. Among the several error sources associated with the pion–proton PID selection, the dominant one is due to the uncertainty in the (small) fraction of pions and protons with an associated anomalous TOFW β measurement, that is a β measurement which exhibits a non-Gaussian behaviour. Estimates of the uncertainty in the kaon contamination and in the correction for the electron veto have been obtained from an analysis of the data as explained in Section 5. The robustness of the pion PID selection and its associated correction has been evaluated by performing the analysis with tighter and looser PID probability cuts with respect to their nominal values, while correcting for the PID efficiency and migration corresponding to the probability cuts.

Fourth, we have included uncertainties associated with the momentum reconstruction performance of the spectrometer, and with the corrections needed to convert the measured momenta to 'true' momenta. Concerning the momentum, biases and resolution effects are taken into account using both real and simulated data. It was found that momentum biases do not exceed the 5% level from a study of beam particles at different momenta and from a comparison between the reconstructed momenta and the momenta inferred from β measurements with the TOFW and the threshold curves in the Cherenkov.

Finally, an overall normalization uncertainty of 4% has been estimated. The dominant sources for this uncertainty are the targeting efficiency uncertainty, which is deduced from the measurement of transverse beam spot size on target, as well as the reconstruction and PID uncertainties that are fully correlated across different (p, θ) pion bins, and which are not included in the above evaluation. On the other hand, the aluminium target thickness and density were carefully measured, and the effect on the overall cross-section normalization due to these uncertainties is negligible.

8.2 Results of the Error Evaluation

The impact of the error sources discussed in the previous section on the final cross-section measurement has been evaluated, either by analytic error propagation, or by Monte Carlo techniques. Correlation effects among different particle types, and among different (p, θ) bins, have also been taken into account.

The cross-section uncertainty level is quantified by adopting two different conventions. The rationale is that both the errors on the 'point–to–point', double-differential cross-section, and the error on the cross-section integrated over the entire pion phase space measured, might be of interest.

Error Category	Error Source	δ_{diff} (%)	δ_{int} (%)
Statistical	Al target statistics	1.6	0.3
	Empty target subtraction (stat.)	1.3	0.2
	Sub-total	**2.1**	**0.4**
Track yield corrections	Reconstruction efficiency	0.8	0.4
	Pion, proton absorption	2.4	2.6
	Tertiary subtraction	3.2	2.9
	Empty target subtraction (syst.)	1.2	1.1
	Sub-total	**4.5**	**4.1**
Particle identification	PID Probability cut	0.2	0.2
	Kaon subtraction	0.3	0.1
	Electron veto	2.1	0.5
	Pion, proton ID correction	2.5	0.4
	Sub-total	**3.5**	**0.7**
Momentum reconstruction	Momentum scale	3.0	0.3
	Momentum resolution	0.6	0.6
	Sub-total	**3.2**	**0.7**
Overall normalization	**Sub-total**	**4.0**	**4.0**
All	**Total**	**8.2**	**5.8**

Table 3: Summary of the uncertainties affecting the double-differential cross-section (δ_{diff}) and integrated cross-section (δ_{int}) measurements. See text for details.

First, the dimensionless quantity δ_{diff} is defined, expressing the typical error on the double-differential cross-section, as follows:

$$\delta_{\text{diff}} \equiv \frac{\sum_i (\delta[\Delta^2\sigma^\pi/(\Delta p \Delta\Omega)])_i}{\sum_i (\Delta^2\sigma^\pi/(\Delta p \Delta\Omega))_i} \ , \tag{15}$$

where i labels a given pion (p, θ) bin, $(\Delta^2\sigma^\pi/(dp \cdot d\Omega))_i$ is the central value for the double-differential cross-section measurement in that bin, and $(\delta[\Delta^2\sigma^\pi/(dp \cdot d\Omega)])_i$ is the error associated with this measurement.

The individual and cumulative effect of the error sources discussed above on the δ_{diff} quantity are shown in Table 3. The typical error on the double-differential cross-section is about 8.2%. The dominant error contributions to δ_{diff} arise from overall normalization (4%), subtraction of tertiary tracks (3.2%), and momentum scale (3.0%). More details on the relative double-differential cross-section uncertainties are shown in Fig. 28 for all measured (p, θ) bins. In Figure 28 and in Tab. 3, the individual cross-section uncertainties are grouped into five categories: statistical, track yield corrections, particle identification, momentum reconstruction, and overall normalization uncertainties. Uncertainties associated with the track yield corrections discussed above dominate the cross-section uncertainties in the low momentum region, while the dominant errors in the high momentum region are due to the momentum reconstruction and to the overall normalization.

Second, we define the dimensionless quantity δ_{int}, expressing the fractional error on the integrated pion cross-section, $\sigma^\pi(0.75 \text{ GeV}/c \leq p < 6.5 \text{ GeV}/c, 30 \text{ mrad} \leq \theta < 210 \text{ mrad})$, as follows:

$$\delta_{\text{int}} \equiv \frac{\sqrt{\sum_{i,j} (\Delta p \Delta\Omega)_i C_{ij} (\Delta p \Delta\Omega)_j}}{\sum_i (\Delta^2\sigma^\pi)_i} \ , \tag{16}$$

where $(\Delta^2\sigma^\pi)_i$ is the double-differential cross-section in bin i, $(\Delta^2\sigma^\pi/(\Delta p \Delta\Omega))_i$, multiplied by its corresponding phase space element $(\Delta p \Delta\Omega)_i$. Here, C_{ij} is the covariance matrix of the double-differential cross-section obtained by summing thirteen matrices from the error sources listed in Table 3, and whose square root of the diagonal elements, $\sqrt{C_{ii}}$, corresponds to the error $(\delta(\Delta^2\sigma^\pi/(\Delta p \Delta\Omega)))_i$ appearing in Eq. 15. This covariance matrix is used to compare the two independent analyses of the same cross-section

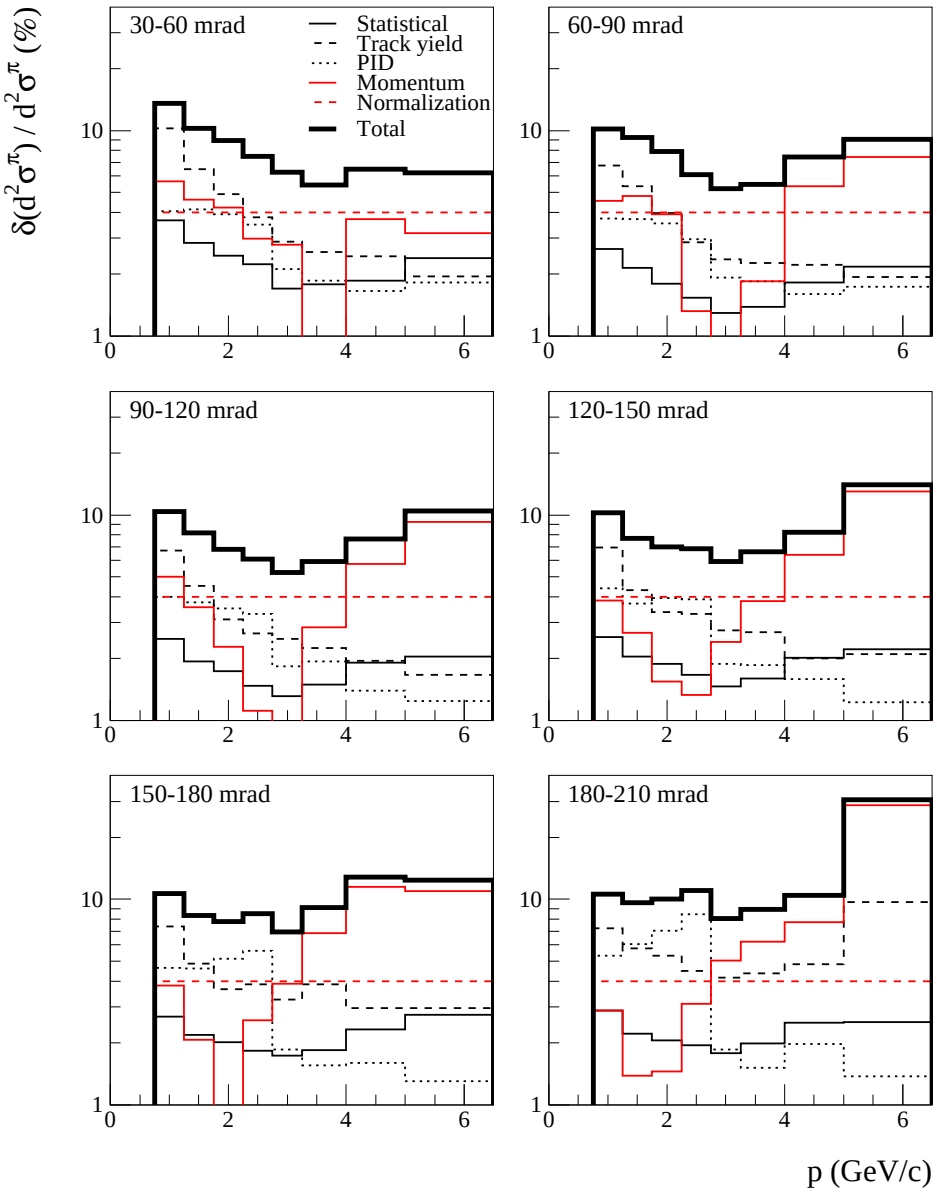

Figure 28: Estimate of the fractional errors on the double-differential pion production cross-section measured as a function of pion momentum p and polar angle. The errors shown are in percent. The contributions from the error categories in Tab. 3 (thin histograms) as well as the total error (thick solid) are shown.

Parameter	Value
c_1	$(4.4 \pm 1.3) \cdot 10^2$
c_2	$(8.5 \pm 3.4) \cdot 10^{-1}$
c_3	(5.1 ± 1.3)
$c_4 = c_5$	(1.78 ± 0.75)
c_6	(4.43 ± 0.31)
c_7	$(1.35 \pm 0.29) \cdot 10^{-1}$
c_8	$(3.57 \pm 0.96) \cdot 10^1$

Table 4: Sanford-Wang parameters and errors obtained by fitting the dataset. The errors refer to the 68.27% confidence level for seven parameters ($\Delta\chi^2 = 8.18$).

measurement, and to obtain the best-fit values, errors, and correlations for the coefficients entering into the Sanford-Wang formula used to parametrize the HARP measurements. The correlation coefficients among distinct (p, θ) bins in C_{ij} vary between -0.19 and $+0.95$.

The contributions to $\delta_{\rm int}$ from all the error sources considered, as well as the total error estimate on the integrated cross-section, are also given in Table 3. As expected, (mostly) correlated errors such as the one from the normalization or tertiary subtraction remain (almost) as large as they were for the point-to-point error. On the other hand, the contribution of the momentum scale uncertainty is negligible here, since its effect tends to be anti-correlated among different phase space bins. In addition to the normalization and tertiary subtraction, other uncertainty sources which have some impact on the integrated cross-section include the pion absorption correction and the empty target subtraction systematic uncertainty. Overall, the total uncertainty on the pion production cross-section measured over the entire phase space ($0.75 \leq p < 6.5$ GeV/c, $30 \leq \theta < 210$ mrad) is estimated to be about 6%.

In the following section, the cross-section results are also expressed in a parametrized form.

8.3 Sanford-Wang parametrization

The π^+ production data was fitted with a Sanford-Wang parametrization [17], which has the functional form:

$$\frac{d^2\sigma(\mathrm{p+A} \to \pi^+ + X)}{dpd\Omega}(p,\theta) = c_1 p^{c_2}(1 - \frac{p}{p_{\rm beam}}) \exp[-c_3 \frac{p^{c_4}}{p_{\rm beam}^{c_5}} - c_6\theta(p - c_7 p_{\rm beam} \cos^{c_8}\theta)] \ , \qquad (17)$$

where X denotes any system of other particles in the final state, $p_{\rm beam}$ is the proton beam momentum in GeV/c, p and θ are the π^+ momentum and angle in units of GeV/c and radians, respectively, $d^2\sigma/(dpd\Omega)$ is expressed in units of mb/(GeV/c sr), $d\Omega \equiv 2\pi \ d(\cos\theta)$, and the parameters $c_1, \ldots, c_8$ are obtained from fits to π^+ production data.

The parameter c_1 is an overall normalization factor, the four parameters c_2, c_3, c_4, c_5 can be interpreted as describing the momentum distribution of the secondary pions, and the three parameters c_6, c_7, c_8 as describing the angular distribution for fixed secondary and proton beam momenta, p and $p_{\rm beam}$. This formula is purely empirical. In the χ^2 minimization procedure, seven out of these eight parameters were allowed to vary. The parameter c_5 was fixed to the conventional value $c_5 \equiv c_4$, since the cross-section dependence on the proton beam momentum cannot be addressed by the present HARP data-set, which includes exclusively measurements taken at $p_{\rm beam} = 12.9$ GeV/c. In the χ^2 minimization, the full error matrix was used.

Concerning the Sanford-Wang parameters estimation, the best-fit values of the Sanford-Wang parameters are reported in Table 4, together with their errors. The fit parameter errors are estimated by requiring $\Delta\chi^2 \equiv \chi^2 - \chi^2_{\rm min}$=8.18, corresponding to the 68.27% confidence level region for seven variable parameters. Significant correlations among fit parameters are found, as shown by the correlation matrix given in Table 5.

Parameter	c_1	c_2	c_3	$c_4 = c_5$	c_6	c_7	c_8
c_1	1.000						
c_2	-0.056	1.000					
c_3	-0.145	-0.691	1.000				
$c_4 = c_5$	-0.322	-0.890	0.831	1.000			
c_6	-0.347	0.263	-0.252	-0.067	1.000		
c_7	-0.740	0.148	-0.067	0.077	0.326	1.000	
c_8	0.130	-0.044	0.205	-0.040	-0.650	0.189	1.000

Table 5: Correlation coefficients among the Sanford-Wang parameters, obtained by fitting the data.

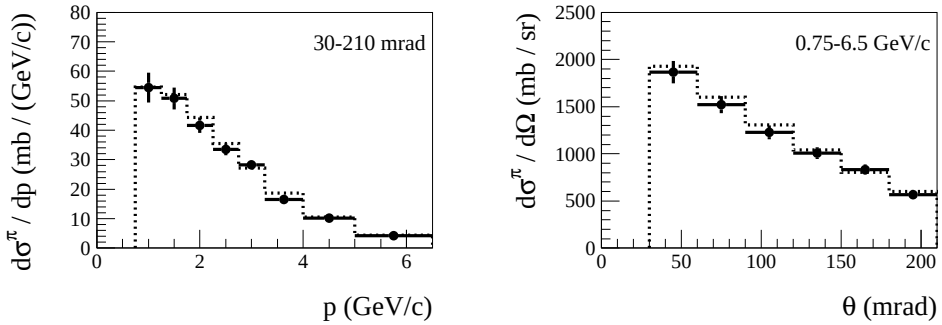

Figure 29: Projections of the differential light hadron production cross-section as a function of p integrated over the range $30 \leq \theta < 210$ mrad (left panel), and production cross-section as a function of θ in the range $0.75 \leq p < 6.5$ GeV/c (right panel). The points show the HARP measurements, the dotted curve the best-fit Sanford-Wang parametrization.

The HARP cross-section measurement is compared to the best-fit Sanford-Wang parametrization of Table 4 in Figs. 27 and 29.

The goodness-of-fit of the Sanford-Wang parametrization hypothesis for the HARP results can be assessed by considering the best-fit χ^2 value of $\chi^2_{\rm min}$=305 for 41 degrees of freedom, indicating a very poor fit quality. We note that the goodness-of-fit strongly depends on the correlations among the HARP cross-section uncertainties in different (p, θ) bins, and therefore cannot be inferred from Fig. 27 alone. If these uncertainties were (incorrectly) treated as completely uncorrelated, the best-fit χ^2 value would decrease from 305 to 57. A more comprehensive study of π^+ production at various beam momenta and from various nuclear targets in HARP is planned and will follow in a subsequent publication, and should hopefully shed more light on the cause of the poor quality of the Sanford-Wang hypothesis reported here.

9 Comparison with existing forward pion production data on aluminium

Finally the HARP results are compared with existing π^+ production data available in the literature directly from aluminium targets [18, 19, 20, 21]. The comparison is restricted to proton beam momenta between 10 and 15 GeV/c (close to the K2K beam momentum of 12.9 GeV/c), and for pion polar angles below 200 mrad (the range measured by HARP and of relevance to K2K).

The comparison is based on the HARP Sanford-Wang parametrization rather than on the HARP data points themselves, in order to match pion momenta and angles measured in past Al experiments. Furthermore, a correction to rescale the HARP Sanford-Wang parametrization at 12.9 GeV/c beam momentum to the 10–15 GeV/c beam momenta of the past Al datasets is applied [22].

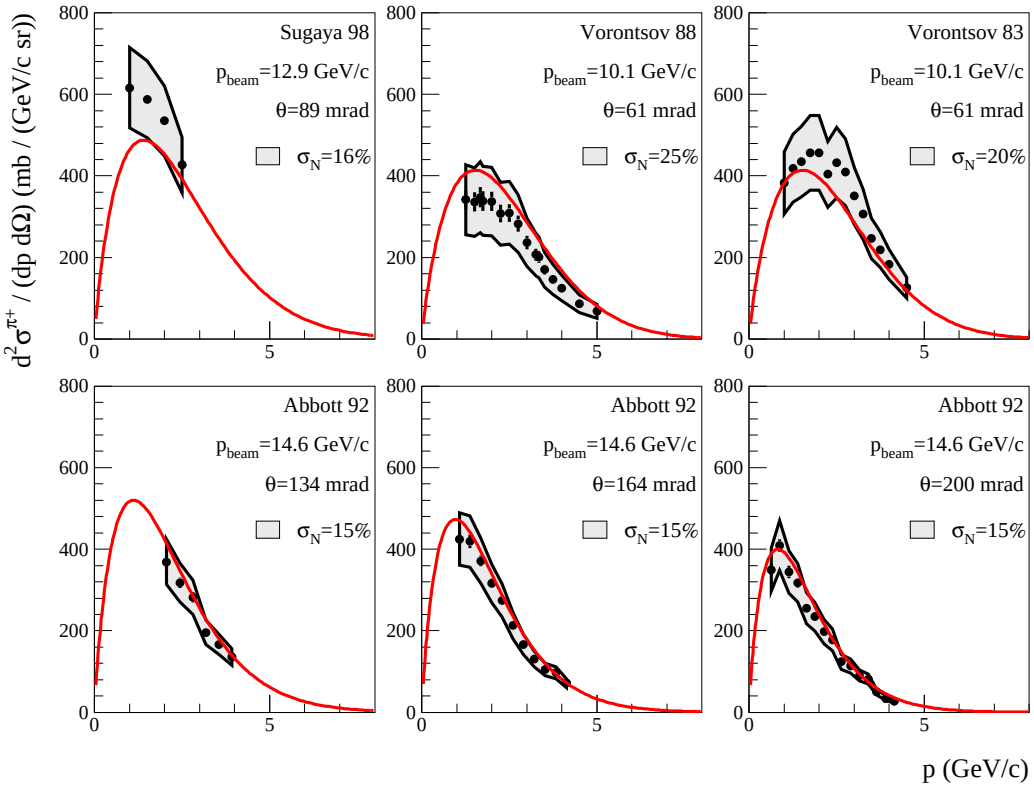

Figure 30: Comparison of the double-differential pion production cross-section measured in HARP, and the one measured in past experiments using an aluminium target and 10-15 GeV/c momentum beam protons. The points are the data from past experiments, and the shaded area reflect their normalization uncertainty. The solid line is the HARP Sanford-Wang parametrization rescaled to the beam momentum of past experiments, as discussed in the text.

Given these model-dependent corrections, it was found that the HARP results are consistent with Ref. [19] and Refs. [20], agree rather well with [21] and are somewhat lower than, but still marginally consistent with, Ref. [18]. Figure 30 shows the comparison between HARP and the above datasets.

10 HARP results as input to the K2K far–to–near neutrino flux ratio prediction

The main application of the measurement presented in this paper, the double-differential π^+ production cross-section, $d^2\sigma\ (p + \mathrm{Al} \to \pi^+ + X)/(dpd\Omega)$, is to predict the far–near ratio, R, for the muon neutrino disappearance search in the K2K experiment.

As discussed in Sec. 1, the determination of the far–near ratio is the leading energy-dependent systematic error in the K2K analysis [2, 3]. To compute this quantity a Monte Carlo program simulating all relevant beam-line geometry and materials, and all relevant physics processes, is used. In this simulation, the neutrino flux prediction uncertainty is dominated by the uncertainties in the forward π^+ production arising from the interactions of the 12.9 GeV/c protons in the aluminium target material. Therefore, it is instructive to recompute a prediction for the K2K far–to–near flux ratio prediction based on the new experimental information presented in this paper. The HARP-based prediction has been obtained by substituting the original π^+ production cross-section assumed in the K2K beam Monte Carlo hadronic model with the HARP Sanford-Wang parametrization discussed in Section 8, while keeping unchanged all other ingredients of the K2K beam MC simulation, such as primary beam optics, pion re-interactions

in the aluminium target, pion focusing, pion decay, etc. More details on the default K2K beam MC assumptions can be found in Ref. [2].

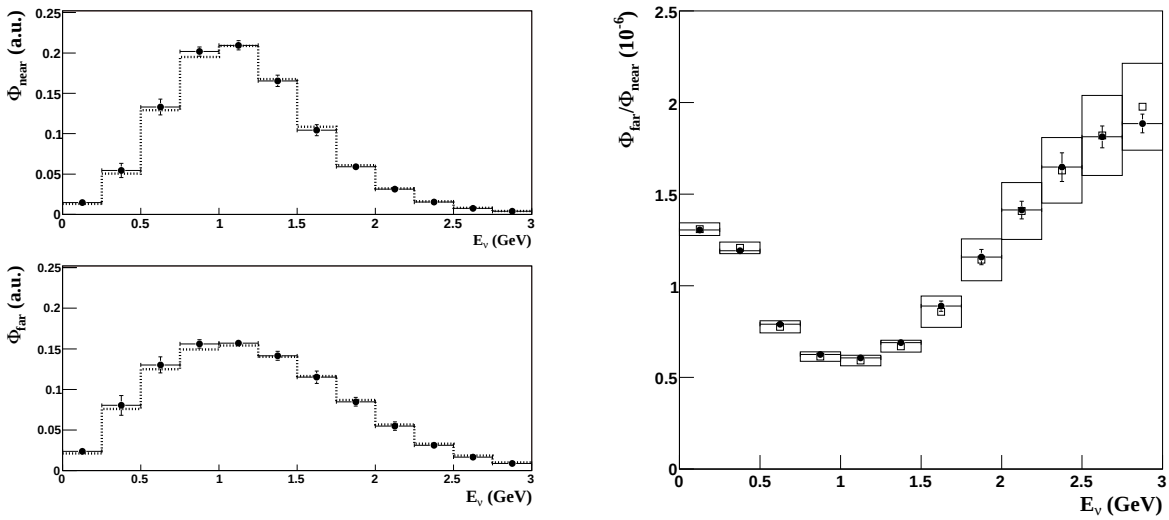

Figure 31: Muon neutrino fluxes in the K2K experiment as a function of neutrino energy E_ν, as predicted by the default hadronic model assumptions in the K2K beam Monte Carlo simulation (dotted histograms), and by the HARP π^+ production measurement (full circles with error bars). Left panel shows unit-area normalized flux predictions at the K2K near (top) and far (bottom) detector locations, $\Phi_{\rm near}$ and $\Phi_{\rm far}$, respectively, while right panel shows the far–to–near flux ratio $\Phi_{\rm far}/\Phi_{\rm near}$ (open squares with error boxes show K2K model results).

The result of this exercise is shown in Fig. 31. The left panel shows muon neutrino fluxes in the K2K experiment as a function of neutrino energy E_ν, as predicted by the default hadronic model assumptions in the K2K beam Monte Carlo simulation (dotted histograms), and by the HARP π^+ production measurement (filled circles). The plots on that panel show unit-area normalized flux predictions at the K2K near (top) and far (bottom) detector locations, $\Phi_{\rm near}$ and $\Phi_{\rm far}$, respectively. Right panel shows the far–to–near flux ratio $\Phi_{\rm far}/\Phi_{\rm near}$ obtained from K2K Monte Carlo (empty squares with error boxes) and from HARP measurament (filled dots with error bars). The fluxes predicted by HARP and the present K2K model are in good agreement within the errors. This is reflected also in a good agreement in R, in particular in the oscillation region (below 1.5 GeV). Finally, it is worth noting that the error on R associated with the HARP measurement (including statistical and systematic errors) is of the order of 1%, since most errors on the cross-section cancel in the ratio. The current systematic error attached to R in the K2K analysis is of the order of 7%. Thus, although the result presented here does not yet represent a new measurement of R (which requires a full evaluation of other systematic errors independent of the HARP measurement but associated with the K2K beam line setup), it clearly shows the considerable improvement that can be achieved by K2K by using this new measurement. In addition, the data taken with the replica of the K2K target will be valuable to study the effect of reinteractions which needs to be taken into account in the beam simulation.

11 Summary and conclusions

In this paper we present a measurement of the double-differential production cross-section $d^2\sigma^{\pi^+}/dpd\Omega$, for positively charged pions. The incident particles are protons of 12.9 GeV/c momentum hitting a thin aluminium target of 5% $\lambda_{\rm I}$. The measurement of this cross-section has a direct application to the calculation of the neutrino flux of the K2K experiment. The data were taken in 2002 in the T9 beam of the CERN PS. Out of 4.7 million triggers processed, 3.4 million incoming protons were selected. After cuts,

around 210 000 secondary tracks reconstructed in the forward spectrometer were used in this analysis. These high statistics results were corrected for measurement resolutions. These data were fitted with a Sanford-Wang parametrization. The results are given for positively charged pions within a momentum range from 0.75 GeV/c to 6.5 GeV/c, and within an angular range from 30 mrad to 210 mrad. The average statistical error is 1.6% per point. The absolute normalization was performed using prescaled beam triggers. The overall efficiency for track reconstruction and particle identification is known to better than 6%, while the average point-to-point error is 8.2%.

12 Acknowledgements

We gratefully acknowledge the help and support of the PS beam staff and of the numerous technical collaborators who contributed to the detector design, construction, commissioning and operation. In particular, we would like to thank G. Barichello, R. Broccard, K. Burin, V. Carassiti, F. Chignoli, G. Decreuse, C. Detraz, M. Dwuznik, F. Evangelisti, B. Friend, A. Iaciofano, I. Krasin, J.-C. Legrand, M. Lobello, F. Marinilli, J. Mulon, R. Nicholson, A. Pepato, P. Petev, X. Pons, I. Rusinov, M. Scandurra, E. Usenko, and R. van der Vlugt, for their support in the construction of the detector. The collaboration is indebted to M. Baldo Ceolin, P. Binko, E. Boter, M. Doucet, D. Düllmann, V. Ermilova, A. Pullia and A. Valassi for their contributions to the experiment.

We are indebted to the K2K collaboration who made available their beam-line simulation for the calculation of the predicted far–to–near neutrino flux ratio.

The experiment was made possible by grants from the Institut Interuniversitaire des Sciences Nucléaires and the Interuniversitair Instituut voor Kernwetenschappen (Belgium), Ministerio de Educacion y Ciencia, Grant FPA2003-06921-c02-02 and Generalitat Valenciana, grant GV00-054-1, CERN (Geneva, Switzerland), the German Bundesministerium für Bildung und Forschung (Germany), the Istituto Nazionale di Fisica Nucleare (Italy), INR RAS (Moscow) and the Particle Physics and Astronomy Research Council (UK). We gratefully acknowledge their support.

References

[1] M.G Catanesi *et al.*, HARP Collaboration, "Proposal to study hadron production for the neutrino factory and for the atmospheric neutrino flux", CERN-SPSC/99-35, 15 November 1999.

[2] M. H. Ahn *et al.* [K2K Collaboration], Phys. Rev. Lett. **90** (2003) 041801 [arXiv:hep-ex/0212007].

S. H. Ahn *et al.* [K2K Collaboration], Phys. Lett. B **511** (2001) 178 [arXiv:hep-ex/0103001].

[3] E. Aliu *et al.* [K2K Collaboration], Phys. Rev. Lett. **94** (2005) 081802 [arXiv:hep-ex/0411038].

[4] Y. Ashie *et al.* [Super-Kamiokande Collaboration], Phys. Rev. D **71** (2005) 112005 [arXiv:hep-ex/0501064].

[5] HARP Collaboration, "The HARP detector at the CERN PS", (*paper in preparation*).

[6] L. Durieu *et al.*, Optic Studies for the T9 Beam Line in the Cern PS East Area Secondary Beam Facility, CERN/PS 2001-037; L. Durieu, O. Fernando, Design of the T9 (ATLAS/CMS) for EHNL, CERN PS/PA Note 96-38.

[7] K. Pretzl *et al.*, Invited talk at the "International Symposium on Strangeness and Quark Matter", Crete, 230 (1999).

[8] J. Altegoer *et al.* [NOMAD Collaboration], Nucl. Instrum. Meth. A **404** (1998) 96.

[9] M. Anfreville *et al.*, Nucl. Instrum. Meth. A **481** (2002) 339 [arXiv:hep-ex/0104012].

[10] M. Baldo-Ceolin *et al.*, Nucl. Instrum. Meth. A **532** (2004) 548.

[11] S. Buontempo *et al.*, Nucl. Instrum. Meth. A **349** (1994) 70.

E. Di Capua *et al.*, Nucl. Instrum. Meth. A **378** (1996) 221.

[12] A. Cervera-Villanueva, J. J. Gomez-Cadenas and J. A. Hernando, Nucl. Instrum. Meth. A **534** (2004) 180.

[13] P. Billoir, Nucl. Instrum. Meth. A **225** (1984) 352.

P. Billoir, R. Fruhwirth and M. Regler, Nucl. Instrum. Meth. A **241** (1985) 115.

R. Frühwirth, Nucl. Instrum. Meth. A **262** (1987) 444.

R. Frühwirth, "Application of Filter Methods to the Reconstruction of Tracks And Vertices in Events of Experimental High Energy Physics", HEPHY-PUB 516/88 Vienna, December 1988.

[14] HARP Collaboration, "Particle identification algorithms for the HARP forward spectrometer", (*paper in preparation*).

[15] G. D'Agostini, Nucl. Instrum. Meth. A **362** (1995) 487.

[16] A. Grossheim, Ph.D. thesis, University of Dortmund, Germany, 2003, CERN-THESIS-2004-010.

[17] J. R. Sanford and C. L. Wang, Brookhaven National Laboratory, AGS internal report, 1967 (unpublished); C. L. Wang, Phys. Rev. Letters 25, 1068 (1970); ibid. 25, 1536(E) (1970).

[18] Y. Sugaya *et al.*, Nucl. Phys. A **634** (1998) 115.

[19] I. A. Vorontsov *et al.*, ITEP-11-1988.

[20] I. A. Vorontsov *et al.*, ITEP-85-1983.

[21] T. Abbott *et al.*, E-802 Collaboration, Phys. Rev. D **45** (1992) 3906.

[22] Y. Cho *et al.*, Phys. Rev. D 4 (1971) 1967.